TU Delft

Delft University of Technology

Cleaner Skies during the COVID-19 Lockdown

Voigt, Christiane; Lelieveld, Jos; Schlager, Hans; Schneider, Johannes; Curtius, Joachim; Bohn, Birger; Mertens, Mariano; Grewe, Volker; Lucke, Johannes; More Authors

DOI
10.1175/BAMS-D-21-0012.1

Publication date
2022

Document Version
Final published version

Published in
Bulletin of The American Meteorological Society

Citation (APA)
Voigt, C., Lelieveld, J., Schlager, H., Schneider, J., Curtius, J., Bohn, B., Mertens, M., Grewe, V., Lucke, J., & More Authors (2022). Cleaner Skies during the COVID-19 Lockdown. *Bulletin of The American Meteorological Society*, *103*(8), E1796-E1827. https://doi.org/10.1175/BAMS-D-21-0012.1

Important note
To cite this publication, please use the final published version (if applicable).
Please check the document version above.

Copyright
Other than for strictly personal use, it is not permitted to download, forward or distribute the text or part of it, without the consent of the author(s) and/or copyright holder(s), unless the work is under an open content license such as Creative Commons.

Takedown policy
Please contact us and provide details if you believe this document breaches copyrights.
We will remove access to the work immediately and investigate your claim.

This work is downloaded from Delft University of Technology.
For technical reasons the number of authors shown on this cover page is limited to a maximum of 10.

BAMS Article

Cleaner Skies during the COVID-19 Lockdown

Christiane Voigt, Jos Lelieveld, Hans Schlager, Johannes Schneider, Joachim Curtius, Ralf Meerkötter, Daniel Sauer, Luca Bugliaro, Birger Bohn, John N. Crowley, Thilo Erbertseder, Silke Groß, Valerian Hahn, Qiang Li, Mariano Mertens, Mira L. Pöhlker, Andrea Pozzer, Ulrich Schumann, Laura Tomsche, Jonathan Williams, Andreas Zahn, Meinrat Andreae, Stephan Borrmann, Tiziana Bräuer, Raphael Dörich, Andreas Dörnbrack, Achim Edtbauer, Lisa Ernle, Horst Fischer, Andreas Giez, Manuel Granzin, Volker Grewe, Hartwig Harder, Martin Heinritzi, Bruna A. Holanda, Patrick Jöckel, Katharina Kaiser, Ovid O. Krüger, Johannes Lucke, Andreas Marsing, Anna Martin, Sigrun Matthes, Christopher Pöhlker, Ulrich Pöschl, Simon Reifenberg, Akima Ringsdorf, Monika Scheibe, Ivan Tadic, Marcel Zauner-Wieczorek, Rolf Henke, and Markus Rapp

ABSTRACT: During spring 2020, the COVID-19 pandemic caused massive reductions in emissions from industry and ground and airborne transportation. To explore the resulting atmospheric composition changes, we conducted the BLUESKY campaign with two research aircraft and measured trace gases, aerosols, and cloud properties from the boundary layer to the lower stratosphere. From 16 May to 9 June 2020, we performed 20 flights in the early COVID-19 lockdown phase over Europe and the Atlantic Ocean. We found up to 50% reductions in boundary layer nitrogen dioxide concentrations in urban areas from GOME-2B satellite data, along with carbon monoxide reductions in the pollution hot spots. We measured 20%–70% reductions in total reactive nitrogen, carbon monoxide, and fine mode aerosol concentration in profiles over German cities compared to a 10-yr dataset from passenger aircraft. The total aerosol mass was significantly reduced below 5 km altitude, and the organic aerosol fraction also aloft, indicative of decreased organic precursor gas emissions. The reduced aerosol optical thickness caused a perceptible shift in sky color toward the blue part of the spectrum (hence BLUESKY) and increased shortwave radiation at the surface. We find that the 80% decline in air traffic led to substantial reductions in nitrogen oxides at cruise altitudes, in contrail cover, and in resulting radiative forcing. The light extinction and depolarization by cirrus were also reduced in regions with substantially decreased air traffic. General circulation–chemistry model simulations indicate good agreement with the measurements when applying a reduced emission scenario. The comprehensive BLUESKY dataset documents the major impact of anthropogenic emissions on the atmospheric composition.

KEYWORDS: Cirrus clouds; Aerosols/particulates; Air pollution; Atmospheric composition; Measurements; COVID-19

https://doi.org/10.1175/BAMS-D-21-0012.1

Corresponding author: Christiane Voigt, christiane.voigt@dlr.de

In final form 21 March 2022

©2022 American Meteorological Society
For information regarding reuse of this content and general copyright information, consult the AMS Copyright Policy.


This article is licensed under a Creative Commons Attribution 4.0 license.

Brought to you by TU DELFT | Unauthenticated | Downloaded 11/07/22 01:10 PM UTC

AFFILIATIONS: Voigt, Hahn, and Tomsche—Deutsches Zentrum für Luft- und Raumfahrt, Oberpfaffenhofen, and Johannes Gutenberg-Universität, Mainz, Germany; **Lelieveld, Schneider, Crowley, Pozzer, Williams, Dörich, Edtbauer, Ernle, Fischer, Harder, Holanda, Krüger, Martin, C. Pöhlker, Pöschl, Reifenberg, Ringsdorf, and Tadic**—Max-Planck-Institut für Chemie, Mainz, Germany; **Schlager, Meerkötter, Sauer, Bugliaro, Erbertseder, Groß, Li, Mertens, Schumann, Bräuer, Dörnbrack, Giez, Jöckel, Marsing, Matthes, Scheibe, and Henke**—Deutsches Zentrum für Luft- und Raumfahrt, Oberpfaffenhofen, Germany; **Curtius, Granzin, Heinritzi, and Zauner-Wieczorek**—Goethe-Universität Frankfurt, Frankfurt, Germany; **Bohn**—Forschungszentrum Jülich, Jülich, Germany; **M. L. Pöhlker**—Max-Planck-Institut für Chemie, Mainz, and Leipzig Institut für Meteorologie, Universität Leipzig, and Leibniz Institut für Troposphärenforschung, Leipzig, Germany; **Zahn**—Karlsruhe Institut für Technologie, Karlsruhe, Germany; **Andreae**—Max-Planck-Institut für Chemie, Mainz, Germany, and Scripps Institution of Oceanography, University of California, San Diego, La Jolla, California; **Borrmann and Kaiser**—Johannes Gutenberg-Universität, and Max-Planck-Institut für Chemie, Mainz, Germany; **Grewe and Lucke**—Deutsches Zentrum für Luft- und Raumfahrt, Oberpfaffenhofen, Germany, and Faculty of Aerospace Engineering, Delft University of Technology, Delft, Netherlands; **Rapp**—Deutsches Zentrum für Luft- und Raumfahrt, Oberpfaffenhofen, and Ludwig-Maximilians-Universität, Munich, Germany

Regulations to limit the spread of the COVID-19 pandemic led to substantial changes in human life, industrial productivity, and mobility, which caused reductions in emissions from industry and ground and airborne transportation (Venter et al. 2020). Hence, the lockdown period offered the unique opportunity to directly measure the effects of reduced pollution emissions on atmospheric composition and thereby challenge our understanding of the anthropogenically perturbed chemical and physical environment (Kroll et al. 2020). The different starting times and types of regulations from the national governments as well as the different chemical and physical processing and hence lifetimes of the emissions caused regionally different evolutions of atmospheric concentrations of individual species. This leads to major uncertainties in the quantitative estimate of emission changes needed to establish emission inventories (Forster et al. 2020). For example, there have been efforts to derive trends in ground transportation in many countries from searches in web-based map platforms (Le Quéré et al. 2020). Guevara et al. (2021) estimated the reduction in primary emissions from different source sectors, such as energy and manufacturing industries and traffic sectors, based on publicly available data [with further data in Copernicus (2020) and Guevara et al. (2020)]. Extrapolating previous emissions to a 2020 business as usual scenario, they derive an average 33% emission reduction of nitrogen oxides (NO_x) in Europe and similar but less reduction for other pollutants (Fig. 1). The transport and the industry sectors were affected differently from lockdown restrictions, with the highest per-sector emission reductions in aviation, whereas the highest total reduction was attributable to road transport (up to about 70% of all sectors, depending on pollutant). Le et al. (2020) compared satellite observations of particulate matter ($PM_{2.5}$), nitrogen dioxide (NO_2), sulfur dioxide (SO_2), and ozone (O_3) during the lockdown in China to prelockdown observations. While reductions in $PM_{2.5}$, NO_2, and SO_2 agree with the trend expected from reduced emissions from transport and industry, enhancements in $PM_{2.5}$ in the Beijing area could only be explained by taking the appropriate meteorology into account. The impact of meteorology, pollution, and other factors on the boundary layer composition and on $PM_{2.5}$ is discussed in many studies (e.g., Chen et al. 2020; Dhaka et al. 2020; Hallar et al. 2021; Karle et al. 2021; Solimini et al. 2021). These

Brought to you by TU DELFT | Unauthenticated | Downloaded 11/07/22 01:10 PM UTC

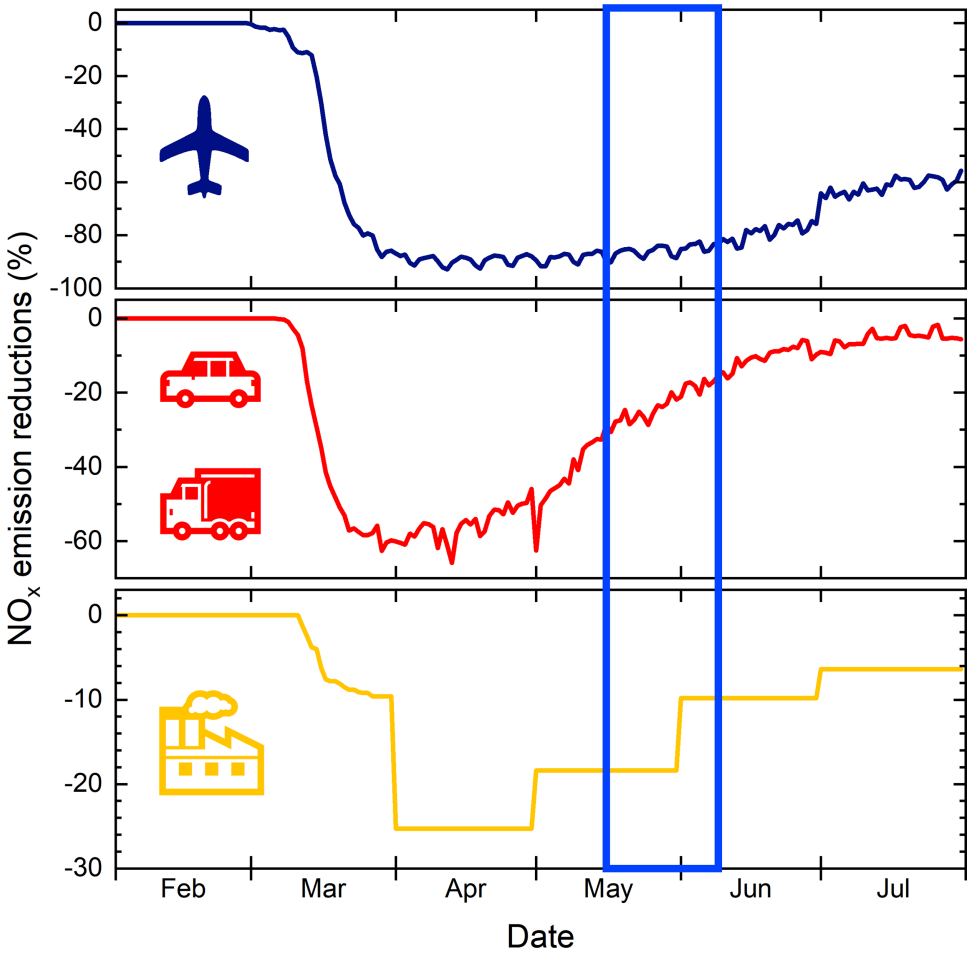


Fig. 1. Percentage change of nitrogen oxide (NO_x) emissions in the aviation (blue), road transport (red), and industry (yellow) sectors in early 2020, compared to a business-as-usual scenario, for the European Union and the United Kingdom. The BLUESKY period was from 16 May to 9 Jun 2020 indicated by the blue box. Emission reduction factors are taken from https://atmosphere.copernicus.eu/covid-data-download [last accessed: 30 Sep 2021; detailed description in Guevara et al. (2020)]. The underlying method has been developed by Guevara et al. (2021).

studies emphasize the need for comprehensive atmospheric composition measurements from the boundary layer to the stratosphere in different parts of the world in order to determine and better understand atmospheric composition changes caused by human activities and distinguish the anthropogenic impact from natural factors.

Travel restrictions resulted in more than 80% reductions in air traffic worldwide during the early lockdown phase (Guevara et al. 2021), and aviation experienced significantly stronger reductions compared to other transport sectors. While air traffic generally recovered within a year in Asia and America, European air traffic lagged behind and showed a significant decrease throughout summer 2020 with a slight recovery toward the end of the year (see Fig. 2). One year after the initial lockdown, European air traffic was still reduced by about 30% compared to pre-COVID-19 levels.

Aircraft emit carbon dioxide (CO_2), nitrogen oxides (NO_x), water vapor (H_2O), and aerosols. The aircraft emissions can modify cirrus clouds and lead to the formation of contrails in cold and humid areas at cruise altitudes (Lee et al. 2010). The recent, comprehensive assessment of air traffic effects on the atmosphere (Lee et al. 2021) shows that aviation up to 2018 contributed about 3.5% to the total anthropogenic effective radiative forcing, with about one-third coming from its CO_2 emissions and two-thirds resulting from the non-CO_2 effects. In fact, the major contributor to effective radiative forcing from aviation is caused by contrail cirrus (57%) (Burkhardt et al. 2018; Lee et al. 2021). The effects of aviation generated aerosol on natural

Brought to you by TU DELFT | Unauthenticated | Downloaded 11/07/22 01:10 PM UTC

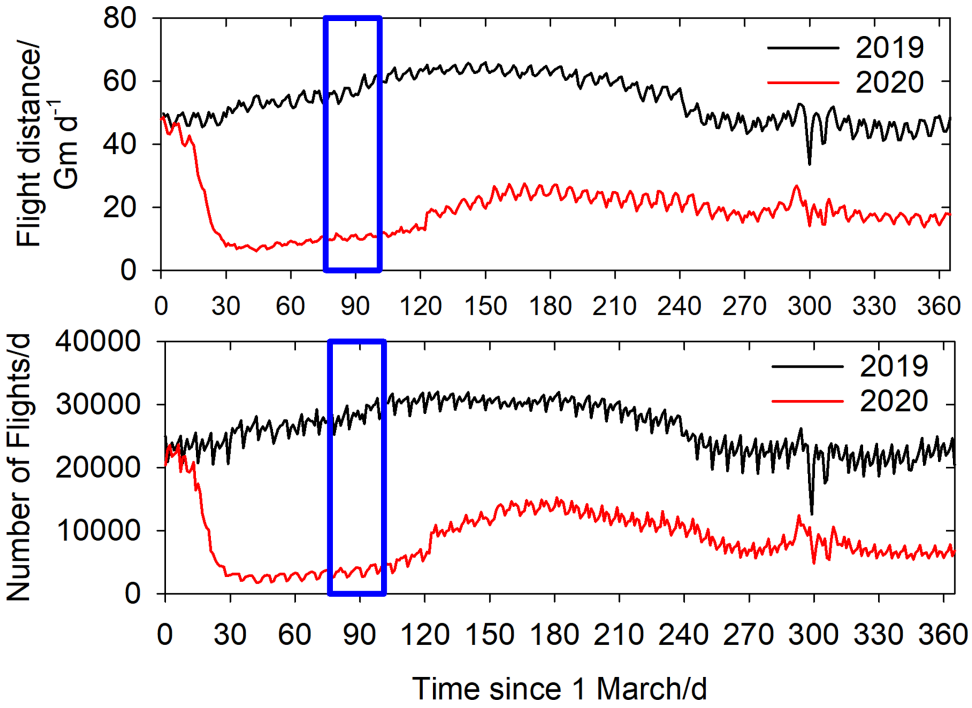


Fig. 2. Flight distance and number of flights over Europe since 1 Mar 2020 (red) and 1 Mar 2019 (black) from EUROCONTROL and NATS. The BLUESKY period was from 16 May to 9 Jun 2020 indicated by the blue box.

clouds remains uncertain (Lee et al. 2021). Properties of contrail cirrus have been measured from aircraft (Heymsfield et al. 2010; Voigt et al. 2010, 2017, 2021; Schumann et al. 2017; Bräuer et al. 2021a,b) and satellites (Minnis et al. 2013; Vázquez-Navarro et al. 2015). These observations were used to evaluate the Contrail Cirrus Prediction model (COCIP) (Schumann 2012; Schumann et al. 2017), with which the radiative forcing from contrail cirrus can be calculated. Reduced contrail cirrus optical thickness and radiative forcing caused by diminished air traffic over Europe has been calculated for a 9-month period in 2020 (Schumann et al. 2021a). Significant reductions in seasonal and regional effective radiative forcing from contrail cirrus caused by reduced air traffic emissions during the lockdown 2020 were also found by Gettelman et al. (2021), while the annual mean effective radiative forcing was less affected. Also, the difficulty in separating the impact of meteorology from the reduced aircraft emissions impact on cloud properties induces considerable uncertainties in the calculations (Schumann et al. 2021b). Quaas et al. (2021) used satellite-based cloud retrievals in regions more and less affected by air traffic to derive changes in the aviation impact on cirrus clouds in 2020. Recent studies (Urbanek et al. 2018; Li and Groß 2021) also suggest changes in optical cirrus properties (extinction, depolarization) caused by aged air traffic emissions. Still, many research questions remain with respect to the derivation of changes in cirrus properties and radiative forcing for reduced air traffic in 2020.

Combined, these challenges motivated the BLUESKY mission (www.dlr.de/content/en/articles/news/2020/02/20200522_bluesky-examines-the-atmosphere-during-the-coronavirus-lockdown.html), with the objective to advance our understanding of the anthropogenic impact on atmospheric composition by acquiring a unique dataset on trace gas, aerosol, and cloud properties measured in the early lockdown phase over central Europe and the northern Atlantic flight corridor. Two aircraft were equipped for the BLUESKY campaign: the High-Altitude and Long-Range Research Aircraft (HALO), a Gulfstream 550 with a range of about 8,000 km and 14.5 km cruise altitude (Tadic et al. 2021; Voigt et al. 2017), and the DLR Falcon with 3,000 km range and up to 12 km cruise altitude (Voigt et al. 2011). For BLUESKY, the aircraft were equipped with instruments that measure long- and short-lived

Brought to you by TU DELFT | Unauthenticated | Downloaded 11/07/22 01:10 PM UTC

trace gases, aerosol, and cloud properties. The aircraft measurements were combined with satellite data of tropospheric NO_2 column densities from the Global Ozone Monitoring Experiment 2 (GOME-2; Munro et al. 2016) and *Sentinel-5P*/Tropospheric Monitoring Instrument (TROPOMI; Veefkind et al. 2012), and with cloud data retrieved from the SEVIRI Imager on the Meteosat Second Generation (MSG) satellite, as well as the Cloud–Aerosol Lidar with Orthogonal Polarization (CALIOP) on the *Cloud–Aerosol Lidar and Infrared Pathfinder Satellite Observations* (*CALIPSO*) (Winker et al. 2010). The measurements were also used to evaluate the global chemistry climate model EMAC (Jöckel et al. 2010) and the global–regional chemistry–climate model MECO(n) (Kerkweg and Jöckel 2012a,b; Mertens et al. 2016).

Due to travel restrictions, BLUESKY was conducted out of the home base in Oberpfaffenhofen (48°5′N, 11°17′E) in southern Germany. The observations were performed in May and June 2020 during the early COVID-19 lockdown phase in Europe. This paper describes the aircraft instrumentation and the campaign strategy supported by satellite and modeling activities, as well as first results and highlights from the BLUESKY mission.

Aircraft preparation and instrumentation

During the first days of the lockdown, we developed the idea to deploy the two aircraft HALO and Falcon to measure the atmospheric composition changes during the COVID-19 lockdown. This required adaptation of the Falcon instrumentation to the new science goals by adding instruments to measure O_3 and NO_y, which are expected to be influenced by anthropogenic emissions. For HALO, the payload that was planned for the mission CAFE-Brazil, originally scheduled for May 2021, was used for the BLUESKY mission. The preparation of both aircraft was performed under special health, distance, and safety regulations, as there was no COVID-19 vaccine available at that time. Instrument certification mainly was done from home, and remote access to instruments was promoted; thereby, instrument automatization was advanced for future campaigns. The flights were performed with a minimum crew and with the same personnel to minimize contacts; see Fig. 3.

Also, the scientific payloads of the two aircraft were complementary. The HALO payload included a comprehensive set of trace gas and aerosol instruments and the Falcon was equipped with a smaller trace gas and aerosol payload and in addition included cloud probes. Basic meteorological sensor systems to measure meteorological parameters and humidity were operated on both aircraft. The aircraft instrumentations for BLUESKY are described in more detail below.

HALO instrumentation

The heavily instrumented HALO aircraft focused on the detection of short- and long-lived trace gases as well as aerosol properties and composition (Fig. 4 and Table 1). To this end, several mass spectrometers were operated on HALO: The chemical ionization–atmospheric pressure interface time-of-flight (CI-APITOF) mass spectrometer was deployed to measure nucleating vapors such as sulfuric acid, methanesulfonic acid, highly oxygenated organic molecules, and naturally occurring ions.

The thermal dissociation iodide–chemical–ionization mass spectrometer (I-CIMS) (Slusher et al. 2004; Dörich et al. 2021) monitors peroxyacetylnitric anhydride (PAN), peroxypropylnitric anhydride (PPN), and other species. A proton transfer time of flight mass spectrometer system monitors several volatile organic compounds (Derstroff et al. 2017) including species like isoprene and monoterpenes, acetonitrile, acetone, and methanol. The gas chromatography mass spectrometer (GC-MS) system collects and separates volatile organic components (VOCs) by gas chromatography and detects them with a quadrupole mass spectrometer with a time resolution of 3.5 min (Bourtsoukidis et al. 2017). The instrument provides information on

Brought to you by TU DELFT | Unauthenticated | Downloaded 11/07/22 01:10 PM UTC



Fig. 3. The BLUESKY experiment was performed with the High-Altitude and Long-Range Research Aircraft (HALO) and the DLR research aircraft Falcon in the early COVID-19 lockdown phase from 16 May to 9 Jun 2020. (top) The instrumentation and the cabin crew of the Falcon.

organohalogen compounds such as methyl chloride, selected alkanes, alkenes, aromatics, and alkyl nitrates as well as isopropylnitrate (IPN).

Measurements of NO and NO_2 were made with the Nitrogen Oxides Analyzer for HALO (NOAH) instrument, a modified instrument from ECO-Physics (Hosaynali Beygi et al. 2011). The Airborne Tropospheric Tracer In situ Laser Absorption (ATTILA) spectrometer measured CO and methane (CH_4) using dual quantum cascade midinfrared laser absorption spectroscopy. The hydrogen oxide radicals OH and HO_2 were measured with the Hydroxyl Radical measurement Unit (HORUS) instrument (Marno et al. 2020) based on the laser-induced fluorescence technique. The Tracer In situ quantum cascade laser absorption spectrometer/Hydrogen and Organic Peroxide (TRIHOP) monitor consists of an infrared-laser absorption spectrometer (Schiller et al. 2008) for in situ measurements of formaldehyde (HCHO) and a dual-enzyme monitor (Hottmann et al. 2020) for the detection of hydrogen peroxides H_2O_2 and ROOH.

In addition, the aerosol composition was measured using a compact time-of-flight aerosol mass spectrometer (C-ToF-AMS; Drewnick et al. 2005; Schmale et al. 2010; Schulz et al. 2018). The C-ToF-AMS analyzes aerosol particles in a diameter range of approximately 50–800 nm and provides quantitative mass concentrations of organic matter, sulfate, nitrate, and ammonium. For aircraft operation, it is equipped with a constant pressure inlet that ensures a steady mass flow and operation pressure of the aerodynamic lens. The Fast Aerosol Size Distribution (FASD) system contains a condensation particle counter (CPC) battery, an Ultra-High Sensitivity Aerosol Spectrometer (UHSAS) instrument, and an optical particle size spectrometer. The CCN-Rack includes a cloud condensation nuclei (CCN) counter (Holanda et al. 2020),

Brought to you by TU DELFT | Unauthenticated | Downloaded 11/07/22 01:10 PM UTC

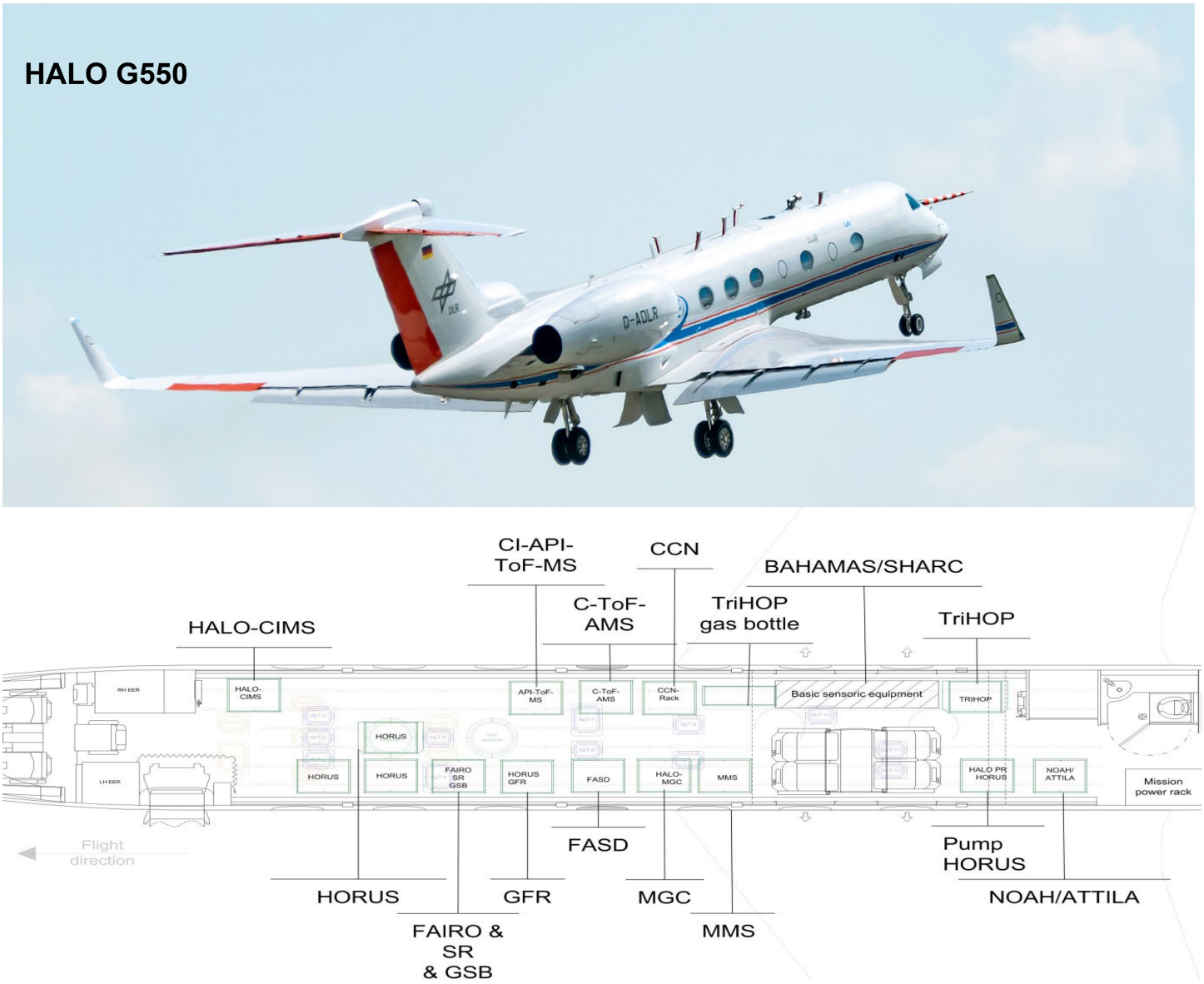


Fig. 4. (top) Photo and (bottom) cabin layout of the comprehensive trace gas and aerosol instrumentation of HALO during BLUESKY.

a single-particle soot photometer (SP2; Krüger et al. 2022; Holanda et al. 2020), and an impaction aerosol sampler with the aim to analyze the physical properties and the chemical composition of aerosol particles. Near isokinetic aerosol sampling was achieved with the HALO Aerosol Submicron Inlet (HASI) mounted on the fuselage outside of the aircraft boundary layer (Andreae et al. 2018).

Finally, upward and downward spectral actinic flux densities in the range 280–650 nm were measured by combinations of CCD spectroradiometers and optical receivers on the aircraft top and bottom fuselage (Bohn and Lohse 2017), and O_3 was measured with the Fast Airborne Ozone (FAIRO) instrument by a combination of two techniques: a UV photometer and a chemiluminescence detector (Zahn et al. 2012).

Falcon instrumentation

The Falcon instrumentation (Fig. 5 and Table 2) included aircraft tracers, stratospheric and tropospheric tracers and, in addition, a dedicated aerosol and cloud payload. The sum of gas-phase reactive nitrogen species (NO_y) was sampled through a rear-facing inlet tube and detected as NO by chemiluminescence after reduction of the reactive odd-nitrogen

Brought to you by TU DELFT | Unauthenticated | Downloaded 11/07/22 01:10 PM UTC

Table 1. HALO instrumentation for BLUESKY. A comprehensive set of instruments or long- and short-lived trace gases and aerosol properties was integrated.

Instrument	Measured property, range	Principal investigator, institution	References
CI-API-ToF MS	H_2SO_4, $(CH_3)SO_3H$, VOCs, clusters, C2 amines, naturally occurring ions	J. Curtius, GU Frankfurt	—
I-CIMS	PAN/PAA/PPN peroxypropionylnitrate	J. Crowley, MPIC	Phillips et al. (2013)
GC-MS	NMVOC, e.g., isopropylnitrate (IPN)	J. Williams, MPIC	Bourtsoukidis et al. (2017)
PTR-MS	OVOC	J. Williams, MPIC	Edtbauer et al. (2020)
TRIHOP	Total hydroperoxides, H_2O_2, HCHO	H. Fischer, MPIC	Hottmann et al. (2020), Schiller et al. (2008)
NOAH/ATTILA	NO, NO_2/CH_4, CO	H. Fischer, MPIC	Tadic et al. (2021)
HORUS	OH/HO_2	H. Harder, MPIC	Marno et al. (2020)
C-ToF-AMS	Submicron aerosol particle composition (nonrefractory)	J. Schneider, MPIC	Drewnick et al. (2005), Schmale et al. (2010), Schulz et al. (2018)
FASD (CPCs, UHSAS, OPC)	Aerosol number and size distribution	M. Pöhlker, MPIC	
CCN-Rack (CCNC, SP2, impactor)	CCN, BC, aerosol impactor	M. Pöhlker/U. Pöschl, MPIC	Andreae et al. (2018), Holanda et al. (2020), Krüger et al. (2022)
FAIRO	O_3	A. Zahn, KIT	Zahn et al. (2012)
HALO-SR	Actinic flux density, 280–650 nm	B. Bohn, FZJ	Bohn and Lohse (2017)
BAHAMAS	Pressure, temperature, wind, humidity, TAS, aircraft position, altitude	A. Giez, DLR	—
SHARC	H_2O mixing ratio (gas phase)	A. Giez, DLR	—

compounds in a heated gold converter (Ziereis et al. 2022). O_3 was measured using an UV photometer (Schulte and Schlager 1996; Ziereis et al. 2000). CO, CH_4, and CO_2 were measured by cavity ring down spectroscopy (Klausner et al. 2020). The instruments were calibrated using standard mixtures which can be traced back to reference standards of the National Institute of Standards and of Global Atmosphere Watch. The accuracies of the measurements are 15% for NO_y and CO, 5% for O_3, 0.1% for CH_4, and 0.02% for CO_2. The atmospheric chemical ionization mass spectrometer (AIMS) uses SF_5^- reagent ions for the detection of upper tropospheric and stratospheric concentrations of gaseous SO_2, hydrogen chloride (HCl), nitric acid (HNO_3), and chlorine nitrate ($ClONO_2$) (Voigt et al. 2014; Jurkat et al. 2016, 2017; Marsing et al. 2019).

Water vapor distribution was measured with the accurate frost point hygrometer CR2 (Voigt et al. 2010; Kaufmann et al. 2014; Heller et al. 2017) and the liquid or ice water content with the tunable diode laser water vapor analyzer (WARAN) instrument (Kaufmann et al. 2018). Aerosol number concentrations were detected with a set of CPCs with different cutoff diameters of 5, 18, and 50 nm facilitated by different temperature settings and diffusion screen separators (Fiebig et al. 2005; Feldpausch et al. 2006) and a Particle Soot Absorption Photometer (PSAP) measuring aerosol optical properties at three wavelengths of 467, 530, and 660 nm (Virkkula et al. 2005; Virkkula 2010).

Two additional aerosol instruments and two cloud probes were installed in wing stations on the Falcon, including the cloud, aerosol, and precipitation probe (CAPS) (Baumgardner et al. 2004; Voigt et al. 2017) and the cloud and aerosol spectrometer with polarization (CAS-DPOL) (Baumgardner et al. 2004; Taylor et al. 2019; Kleine et al. 2018), as well as two optical particle spectrometers, the UHSAS and Passive Cavity Aerosol Spectrometer Probe (PCASP) (Voigt et al. 2021).

BLUESKY flight strategy and scope

After approximately 6 weeks of aircraft and payload preparation, the Falcon took off for the first instrument test flight on 16 May 2020. The first HALO instrument test flight followed 5 days later.

Brought to you by TU DELFT | Unauthenticated | Downloaded 11/07/22 01:10 PM UTC

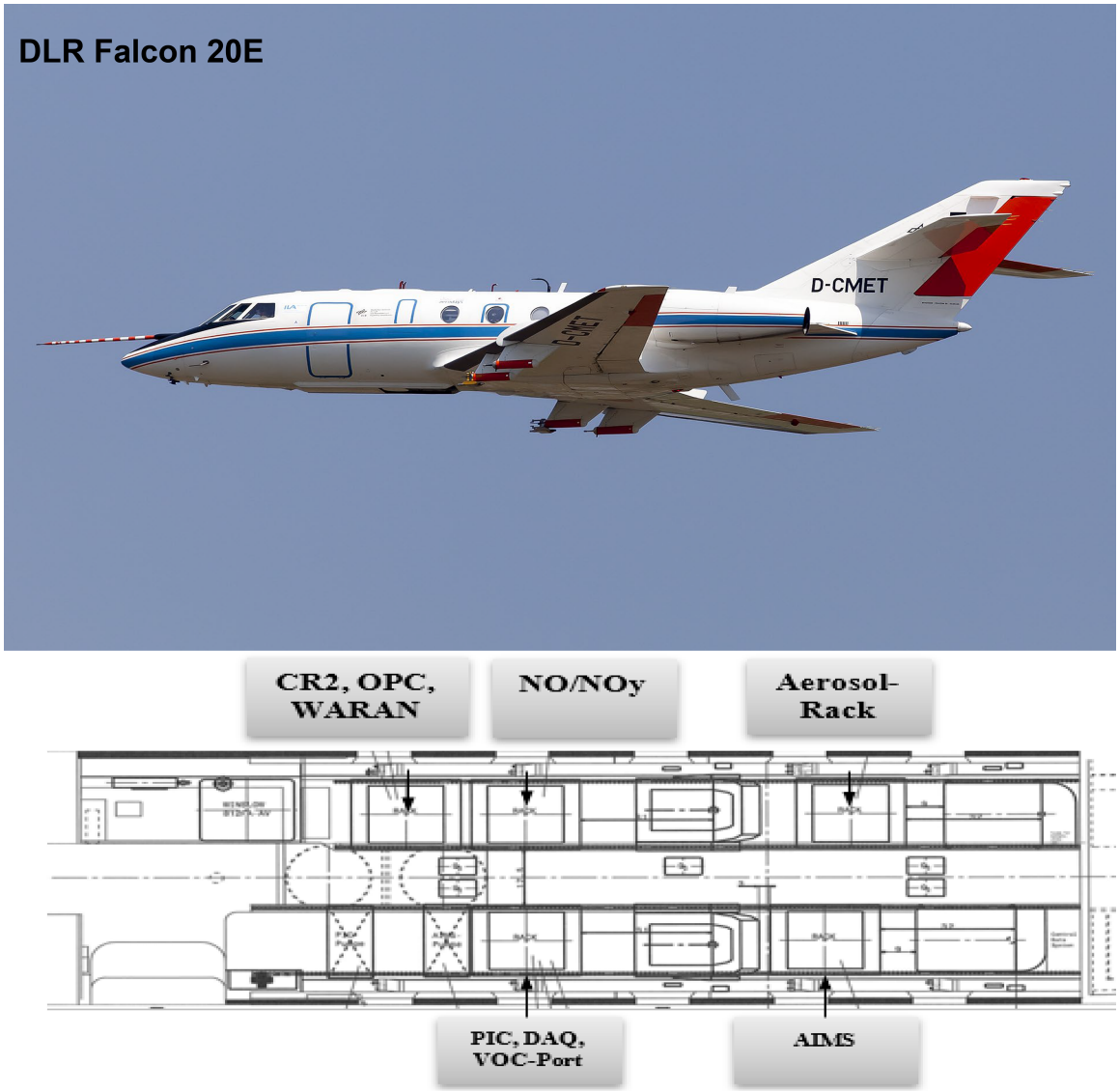


Fig. 5. (top) Photo and (bottom) cabin layout of the trace gas, aerosol, and cloud instrumentation of the DLR Falcon 20 E during BLUESKY.

Both aircraft flew five missions together, then the Falcon had to return for maintenance while HALO continued with three more mission flights until 9 June 2020. Altogether 20 flights were performed during BLUESKY, 12 with the Falcon and 8 with HALO, albeit with different flight lengths of up to 2,860 km with the Falcon and up to 6,734 km with HALO, see also Table 3.

Extensive measurements were performed over Germany, western Europe, and the Atlantic from 13°E to 14°W and from 38° to 55°N as shown in Fig. 6. During survey flights, many profiles of atmospheric composition were made near large cities.

The strict travel restrictions led to strongly reduced air traffic and the DLR research aircraft were for the first time allowed to perform low-approach maneuvers down to 3 m altitude above ground at large international passenger airports like Frankfurt, Berlin-Tegel, and Milan, as well as Amsterdam, Barcelona, Madrid, Marseille, and Rome.

Many profiles were measured near large cities and the composition of the atmosphere was probed from the boundary layer to the lower stratosphere. We also measured spatially highly resolved data of a multitude of trace species in the upper troposphere and lower stratosphere, in order to investigate changes in atmospheric composition caused mainly by aviation. Observations of the reactive nitrogen and ozone distributions in the northern Atlantic flight corridor and over Europe were performed. According to Eurocontrol, during normal operation in 2019, up to 25,000

Brought to you by TU DELFT | Unauthenticated | Downloaded 11/07/22 01:10 PM UTC

Table 2. Falcon instrumentation for BLUESKY. A suite of advanced trace gas, aerosol, and cloud probes was integrated into the cabin and wing stations.

Instrument	Measured property, range	Principal investigator, institution	References
NO_y chemiluminescence detector	NO_y, aircraft tracer, 5 ppt–60 ppb	Schlager, DLR	Schulte and Schlager, (1996), Ziereis et al. (2000, 2021)
UV absorption photometer	O_3	Schlager, DLR	Schlager et al. (1997)
Cavity ring down instrument	CO_2, CH_4, CO	Schlager, DLR	Klausner et al. (2020)
AIMS chemical ionization mass spectrometer	HNO_3, HONO, SO_2, HCl, 5 ppt to 5 ppbv	Voigt, Jurkat, DLR	Voigt et al. (2014), Jurkat et al. (2016, 2017)
CR2, Frostpoint hygrometer	H_2O, gas phase water, 1–1,000 ppm	Heller, DLR	Voigt et al. (2010), Heller et al. (2017)
WARAN, TDL hygrometer	H_2O, total water, 50–40,000 ppm	Heller, DLR	Voigt et al. (2011), Kaufmann et al. (2018)
Aerosol rack with CPCs, OPCs, PSAP	Size distribution of total and nonvolatile aerosol, 4 nm–2 μm, absorption	Sauer, DLR	Fiebig et al. (2005), Voigt et al. (2021)
Meteorological Sensor System	Temperature, u and v wind components, meteorological and aircraft state parameters	Mallaun, DLR	
AIMS, HNO_3, SO_2, HCl mass spectrometer	H_2O, gas-phase water, 1–500 ppm	Voigt/Kaufmann, DLR	Jurkat et al. (2017), Marsing et al. (2019)
CAS-DPOL Cloud and Aerosol Spectrometer	Particle size distribution, polarization, 0.6–50 μm	Voigt, DLR	Voigt et al. (2011), Kleine et al. (2018), Voigt et al. (2021)
CAS-DPOL/CIP (CAPS) Cloud and Aerosol Spectrometer	Particle size distribution, shape, polarization, CAS 0.6–50 μm; CIP 15–960 μm	Voigt, DLR	Voigt et al. (2017), Kleine et al. (2018)
PCASP-100X Passive Cavity Aerosol Spectrometer Probe	Aerosol size distribution, 0.12–3.5 μm	Sauer, DLR	Voigt et al. (2017)
UHSAS Ultra-High-Sensitivity Aerosol Spectrometer	Dry particle size distribution 60–1,000 nm	Sauer, DLR	Voigt et al. (2017)

flights were performed per day in Europe (Fig. 2). The number of flights was greatly reduced, by more than 80%, in the early lockdown phase and gradually recovered to a reduction of about 30% in summer 2021. This also allowed investigation of aviation induced changes in properties of cirrus cloud as observed from satellite. A third specific focus was the effect of shutdown on strongly populated industrial areas like the Ruhr area in Germany and the Milan region in Italy. In both of them, NO_2 levels were strongly enhanced, as urban emissions are captured in a river valley and therefore the exchange with the free-tropospheric air masses is reduced. Satellite observations of tropospheric NO_2 from GOME-2 and TROPOMI are presented in the next section.

Tropospheric NO_2 changes in early lockdown phase during BLUESKY 2020

Tropospheric NO_2 is a representative short-lived tracer for anthropogenic emissions from transport, industrial processes, and energy production (Müller et al. 2022). While the transport sector and in particular diesel engines are often the prevailing source of nitrogen dioxide in the boundary layer, there are also natural emissions from soil (Lu et al. 2021) and lightning (Pérez-Invernón et al. 2022) that can contribute to the boundary layer NO_2 concentrations. Here we use satellite observations from the GOME-2 (Munro et al. 2016) and the TROPOMI (Veefkind et al. 2012) instruments to motivate the BLUESKY campaign, to give a general overview on the changes of the short-lived tracer NO_2 and to support the planning of individual flight tracks. TROPOMI aboard *Sentinel-5 Precursor* (2017 to the present) is a nadir-scanning spectrometer with an equator crossing time at 1330 local solar time and daily global coverage. Retrievals of tropospheric NO_2 vertical column densities have a spatial resolution of 3.5 km × 5.5 km (van Geffen et al. 2019). Each orbit (level 2 products of version 1.2) was sampled onto a grid of 0.01° × 0.01° longitude–latitude resolution to enable a consistent averaging and data

Brought to you by TU DELFT | Unauthenticated | Downloaded 11/07/22 01:10 PM UTC

Table 3. Overview of the BLUESKY flights of Falcon and HALO. Flight number, date, scope, target region, and flight duration are given. The Falcon flights extend from the surface to 12 km altitude and the HALO flights to 14 km altitude.

Flight No.	Date	Takeoff (UTC)	Landing (UTC)	Scope and target region	Length (km)
Falcon0	16 May 2020	0855	1145	Allgäu, Munich area	1,490
F1	19 May 2020	1045	1505	Survey of Germany, boundary layer Ruhr area: Düsseldorf, Hohenpeißenberg, Munich	2,265
F2	21 May 2020	0820	1230	Survey Germany, profiles near Berlin, Hamburg, Frankfurt, Munich	2,259
F3	22 May 2020	1030	1445	Survey Germany: Berlin, Hamburg, Köln, Frankfurt, Munich	2,227
F4	23 May 2020	0850	1130	Survey Germany: profile Berlin, Hamburg	1,508
F5	23 May 2020	1230	1540	Survey Germany, Ruhr area: Hamburg, Köln, Frankfurt, Munich	1,644
F6	26 May 2020	0950	1420	Boundary layer Milano, Italy, Switzerland, Munich	2,262
F7	28 May 2020	0740	1145	Survey Germany: Berlin, Hamburg, Frankfurt, Munich	2,145
F8	30 May 2020	0705	1120	Transfer Ireland, intercomparison HALO, North Atlantic flight tracks (NAT)	2,764
F9	30 May 2020	1210	1650	Shannon, NAT tracks, Munich, Hohenpeissenberg	2,860
F10	1 Jun 2020	0940	1355	Boundary layer Milano, Italy, Switzerland, Munich	2,097
F11	2 Jun 2020	0655	1115	Transfer Ireland, intercomparison HALO, NAT tracks, Shannon	2,798
F12	2 Jun 2020	1205	1620	Shannon, NAT tracks, intercomparison Munich	2,816
HALO 0	21 May 2020	1331	1622	TRA Allgäu, Munich area	1,404
H1	23 May 2020	0806	1439	Berlin, Frankfurt, Hamburg, Köln, Munich area	4,077
H2	26 May 2020	0759	1549	Berlin, Frankfurt, boundary layer Milan, Munich area	4,412
H3	28 May 2020	0804	1515	Berlin, Frankfurt, Hahn, Hamburg, Amsterdam, Köln, Munich area	3,874
H4	30 May 2020	0740	1622	NAT tracks	6,734
H5	2 Jun 2020	0726	1535	NAT tracks	6,436
H6	4 Jun 2020	0801	1620	France (Clermont-Ferrand, Marseille), Mediterranean Sea, Italy (Rome, Adriatic Sea, Milano)	4,738
H7	6 Jun 2020	0757	1537	France (Clermont-Ferrand, Marseille), Spain (Madrid, Barcelona)	4,374
H8	9 Jun 2020	0758	1535	France (Bordeaux, Marseille), Spain (Madrid, Mallorca)	4,652

comparison (Müller et al. 2022). Although observations from TROPOMI currently exhibit the highest spatial resolution to study regional effects on the atmospheric composition the data are available from April 2018 onward only and not yet suitable to examine longer-term variability.

To better analyze the deviation of tropospheric NO_2 levels in 2020 from previous years, GOME-2 data were examined from 2015 to 2020. GOME-2 aboard *MetOp-B* (2012 to the present) is a nadir-scanning spectrometer, which measures at around 0930 local solar time equator crossing time and has a ground pixel size of 80 km × 40 km (Munro et al. 2016). Level 2 offline products of version 4.8 were sampled onto a grid of 0.25° × 0.25° geographical resolution.

Long-term analyses of global satellite data show that NO_2 pollution can vary strongly from year to year due to weather conditions (Zhou et al. 2012; Georgoulias et al. 2019). To reduce this source of variability and uncertainty, observations from GOME-2B for 2020 are compared to the mean from 2015 to 2019 as reference (Fig. 7). For each year the BLUESKY period was considered accordingly. Although the multiannual mean provides a better statistical baseline to quantify possible lockdown effects in 2020, the 3-week sampling period is still short regarding meteorological variability Reductions in tropospheric NO_2 are evident throughout Europe, the United States, and Asia (Fig. 7). The global mean values for the BLUESKY period suggest a 12% reduction in global NO_2 in 2020 with respect to the 2015–19 average. Large cities and conurbations show the highest reductions in NO_2 of up to 55%.

Brought to you by TU DELFT | Unauthenticated | Downloaded 11/07/22 01:10 PM UTC

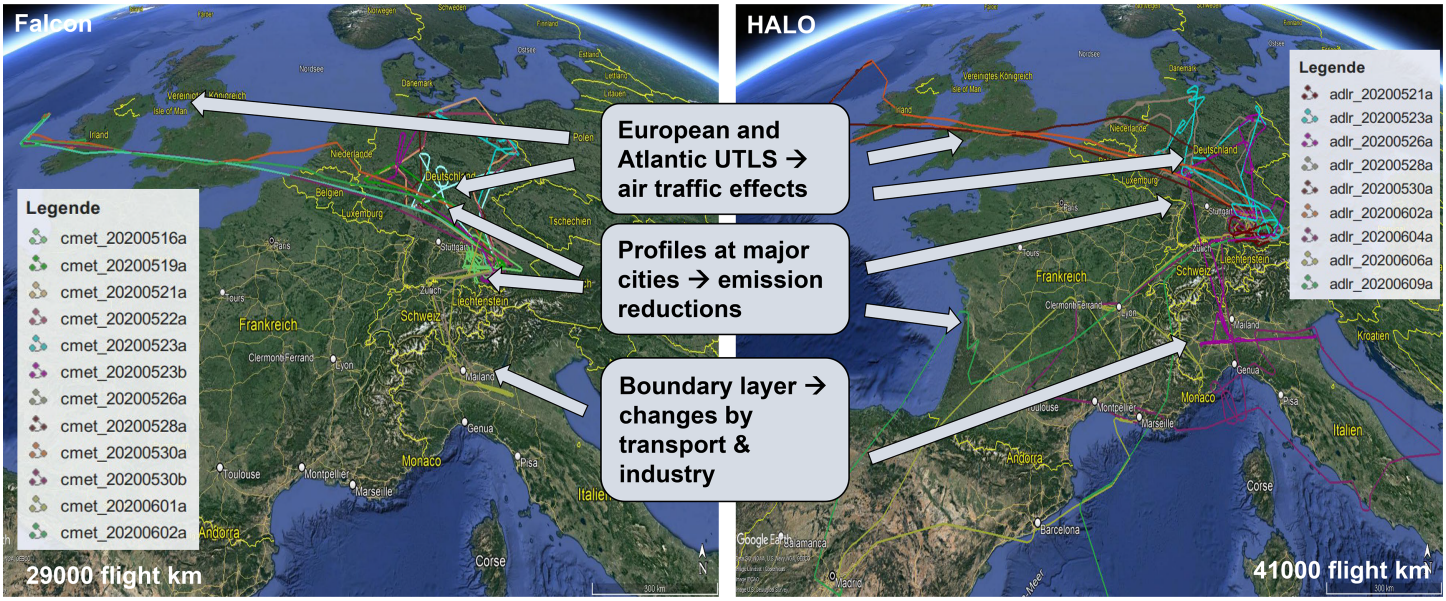


Fig. 6. Scope and flight path of HALO and Falcon during BLUESKY. In order to probe the atmospheric composition during the COVID-19 lockdown, 41,000 km were flown by HALO and 29,000 km by the Falcon from 16 May to 9 Jun 2020.

In Germany, the measures to limit the spread of the coronavirus started with strong social restrictions and a first lockdown on 22 March 2020. On 15 April 2020, the German government decided to gradually reopen public life. In terms of NO_2 levels, a strong reduction was detected from 22 March to 15 April 2020, and from 15 April the NO_2 levels increased gradually (Erbertseder and Loyola 2020).

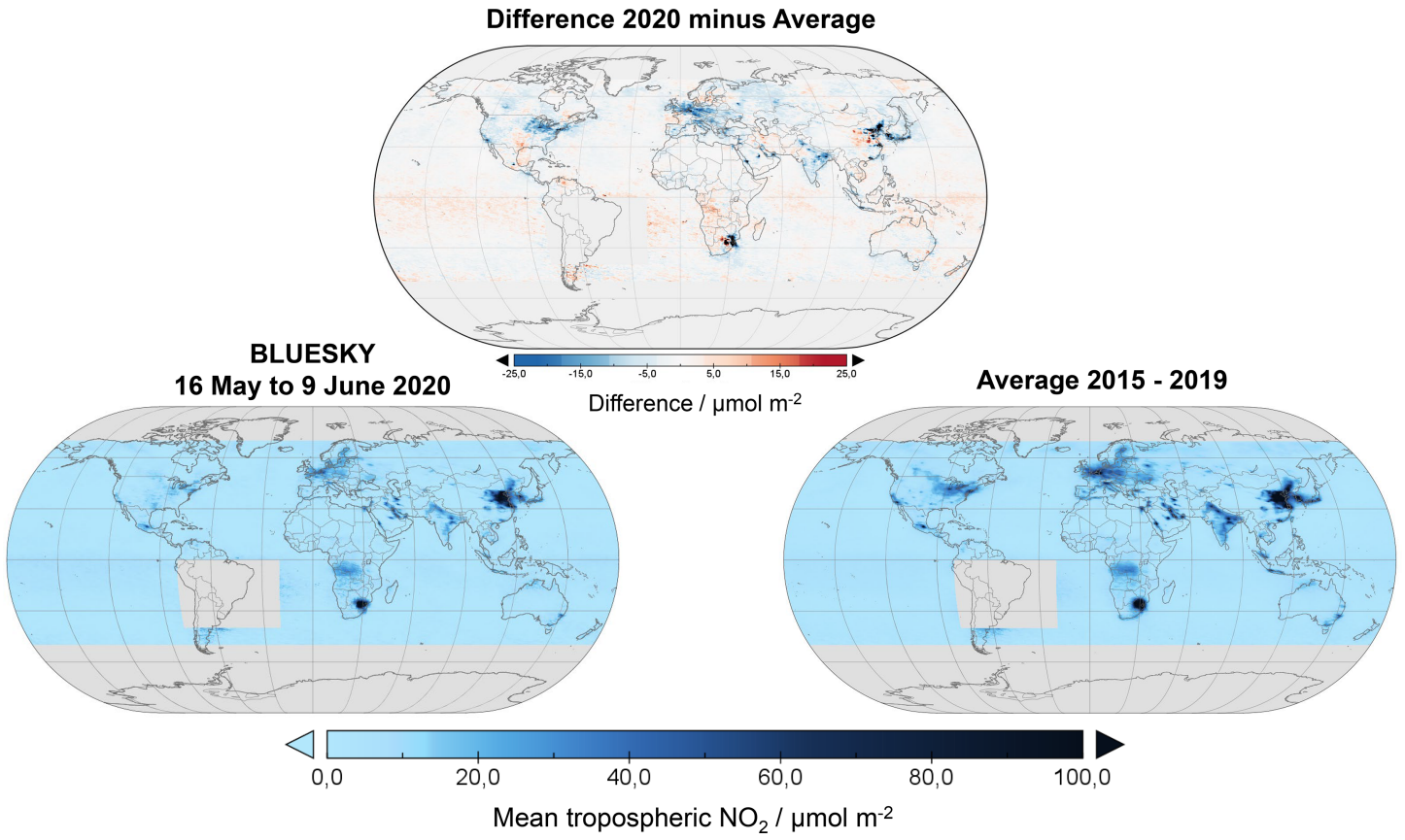


Fig. 7. (top) Differences in tropospheric NO_2 between 2020 and the baseline mean 2015–19 during the BLUESKY period from 16 May to 9 Jun 2020 as observed by MetOp/GOME-2B. (bottom) The averages for the corresponding periods. The area of the South Atlantic anomaly covering large parts of South America is masked.

Brought to you by TU DELFT | Unauthenticated | Downloaded 11/07/22 01:10 PM UTC

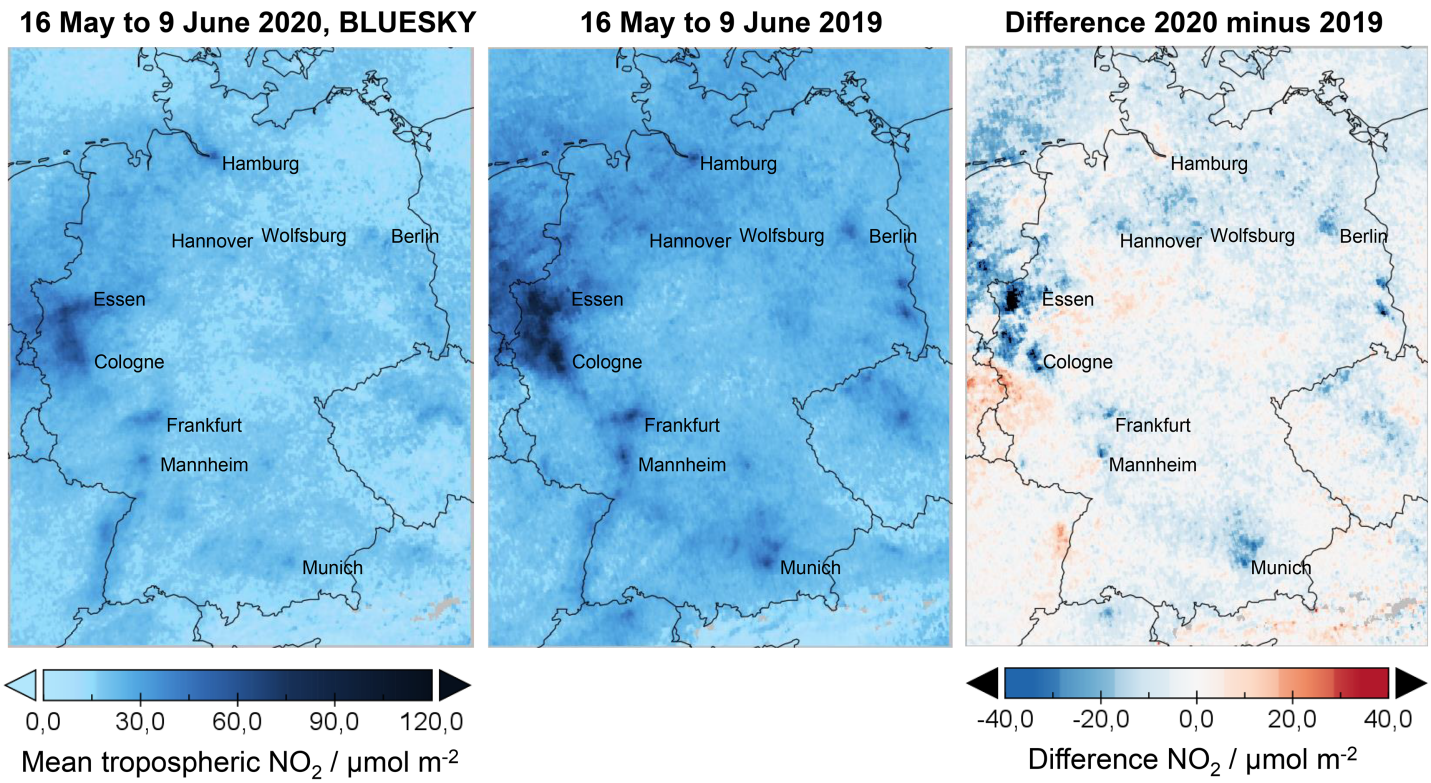


Fig. 8. Mean tropospheric NO_2 vertical column densities over Germany for (left) 2020 and (center) 2019 averaged over the BLUESKY period from 16 May to 9 Jun. The means were derived from *Sentinel-5P*/TROPOMI level 2 data. (right) The difference of 2020 minus 2019.

Tropospheric NO_2 densities monitored by *Sentinel-5P*/TROPOMI overpasses in 2019 and 2020 were used to support the flight planning. Figure 8 shows mean tropospheric NO_2 densities for 2020 and 2019 averaged over the respective BLUESKY period from 16 May to 9 June 2020. For the selected area, the mean NO_2 values are 26.8 ± 8.9 μmol m^{-2} and 31.7 ± 11.2 μmol m^{-2} for 2020 and 2019, respectively. The reduction in 2020 is evident throughout Germany and corresponds to an overall decrease of tropospheric NO_2 in 2020 by about 15%. The decrease is pronounced in the Ruhr area and in urban areas such as Cologne, Frankfurt, Munich, and Berlin with reductions between 21% and 38%, attributable to strongly reduced road traffic and industrial production, but also to lower NO_2 levels in 2020 before the lockdown and meteorological conditions that are not further disentangled here. A detailed analysis of the lockdown effects on tropospheric NO_2 and their statistical significance considering source attributions of different sectors (Petit et al. 2021; Feng et al. 2021; Putaud et al. 2021), adjustments to multiannual trend effects (Bekbulat et al. 2020), or corrections for meteorological influences (Zhou et al. 2012; Goldberg et al. 2020) is out of scope of this paper. However, the presented findings are in the range of more detailed studies that consider wind corrections and adjustments to trend effects, but focus on different periods of the lockdown (e.g., Liu et al. 2020; Goldberg et al. 2020).

Highlights from the BLUESKY mission

We briefly present first results from the BLUESKY mission and show tropospheric profiles of trace species and aerosol affected by anthropogenic emissions, investigate the blue color of the sky and address effects from reduced air traffic on cirrus.

Reduced reactive nitrogen and carbon monoxide in Frankfurt city profiles and in the industrial boundary layer. Profiles taken over Frankfurt can be compared to climatological datasets measured by instrumented in-service passenger aircraft starting or landing in Frankfurt.

Brought to you by TU DELFT | Unauthenticated | Downloaded 11/07/22 01:10 PM UTC

Figure 9 shows vertical profiles of NO_y, CO, and O_3 mixing ratios measured in the Frankfurt area by the Falcon on 28 May 2020 and related model results. The profiles are compared to median profiles derived from a climatology of 11 years of Measurement of Ozone and Water Vapor by Airbus In-Service Aircraft (MOZAIC) measurements at the same time of year (Petzoldt 2010). The MOZAIC dataset includes over 3,000 vertical profiles over Frankfurt covering a multitude of different meteorological situations in the same season. For comparison, average vertical profiles of CO and O_3 sampled by In-service Aircraft for a Global Observing System (IAGOS) in March–May during 2016–19 over Frankfurt at altitudes between 2 and 8 km (Clark et al. 2021) are also shown.

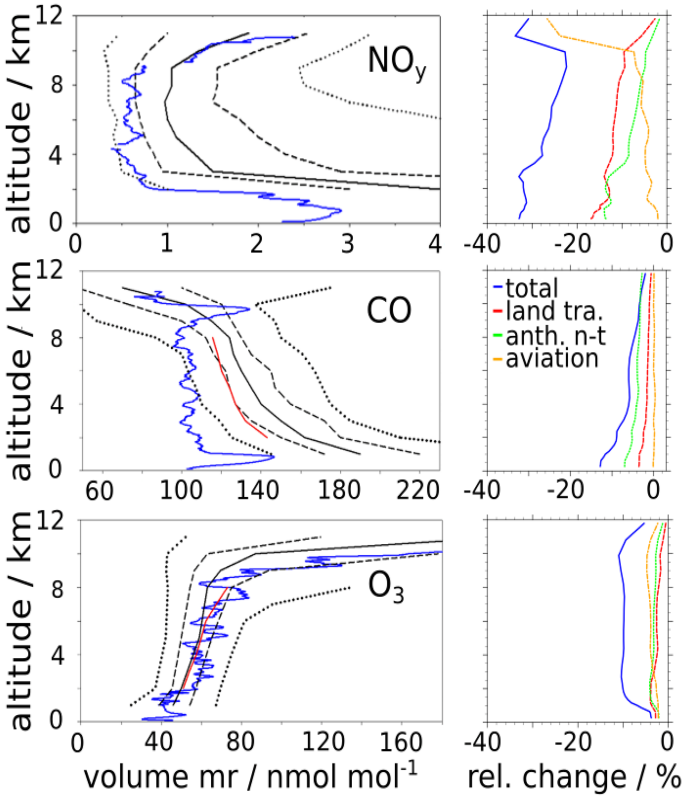


Fig. 9. (left) Vertical profiles of (top) NO_y, (middle) CO, and (bottom) O_3 measured during BLUESKY on 28 May 2020 in the Frankfurt area (blue lines), medians (black solid lines), and 5th, 25th, 75th, and 95th percentiles (black dotted lines) of Frankfurt profile data in spring from a climatology of MOZAIC data sampled from 1994 to 2005 (Petzoldt 2010) and average CO and O_3 profiles over Frankfurt from IAGOS (red lines) for spring 2016–19 (Clark et al. 2021). (right) Vertical profiles of the relative changes (%) for (top) NO_y, (middle) CO, and (bottom) O_3 between the COVID-19 and the business-as-usual simulation over the Frankfurt area at 1000 UTC 28 May. The blue line shows the total change, and red, green, and orange indicate the changes attributed to the emission categories land transport (land tra.), anthropogenic nontraffic (anth. n-t), and aviation, respectively.

The measured NO_y and CO mixing ratios in the lower and middle troposphere are significantly lower than the median MOZAIC values by 40%–70% and 20%–40%, respectively, and the CO mixing ratios are also lower than the average IAGOS CO profile. The observed O_3 concentrations agree with the median MOZAIC and IAGOS profiles. BLUESKY NO_y and CO concentrations over Frankfurt, however, are close to the 5th percentiles, and only 5% of the MOZAIC data are lower than the BLUESKY profiles. These differences can in part be caused by the meteorological conditions prevailing in May and June 2020 and by COVID-19 emissions reductions.

To better distinguish emission reductions from other factors, we add simulated vertical profiles on the right side of Fig. 9, which show the relative difference between a business as usual simulation and a COVID-19 simulation with a reduced emission scenario [see Mertens et al. (2020) for a full description of the simulations] of NO_y, CO, and O_3 mixing ratio around Frankfurt as simulated by MECO(n). Besides the total difference, the differences attributed to the emission sources land transport, anthropogenic nontraffic, and aviation are shown. In fact, the COVID-19 emission reductions assumed in the model simulations lead to a reduction of O_3 of up to 10%, for CO of up to 13%, and for NO_y of up to 34%. The NO_y reduction near ground are mainly due to reduction of land transport emissions, while reductions above 10 km are mainly attributed to changes of aircraft emissions. This indicates that the observed lower NO_y and CO mixing ratios over Frankfurt can to a large extent be attributed to the reduction

Brought to you by TU DELFT | Unauthenticated | Downloaded 11/07/22 01:10 PM UTC

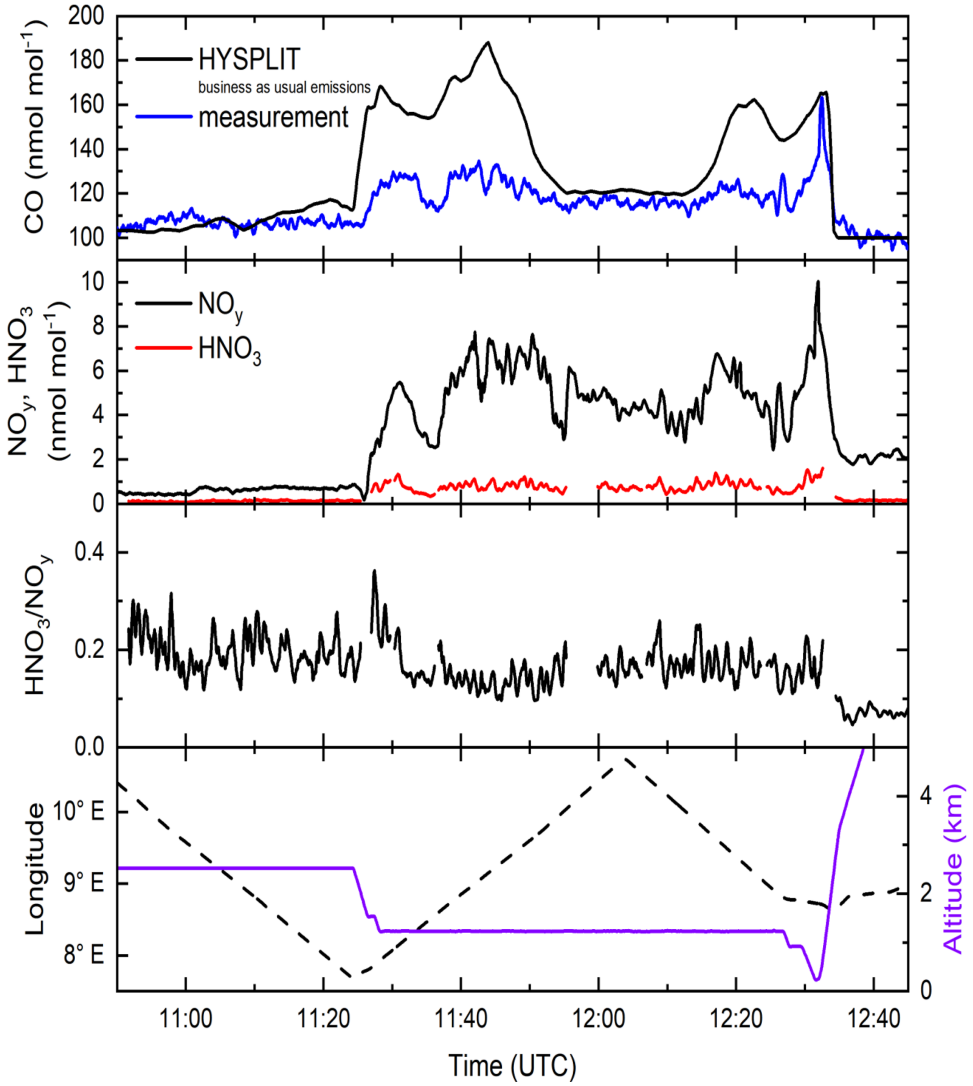


Fig. 10. (top) Falcon measurements of CO volume mixing ratios in the western part of the industrial Po valley near Milan in Italy (blue) on 1 Jun 2020 compared to HYSPLIT simulations with business as usual emissions (black). (middle) Falcon measurements of NO_y and HNO_3 and the relative fraction of HNO_3 in the total gaseous reactive nitrogen budget. (bottom) Longitude (black dashed) and altitude (violet) of the Falcon flight path, indicating the east–west shuttle with vertical steps, terminating in a low approach at the Milan Malpensa airport.

of emissions from the transport sector (land transport and aviation) and to anthropogenic nontraffic COVID-19 emission reductions.

It is interesting to note, that the mixing ratios of the IAGOS average CO profile for the years 2016–19 are about 7% lower than the MOZAIC average profiles for the years 1994–2005, which corresponds to the observed rate of decrease in CO in the Northern Hemispheric troposphere (Clark et al. 2021). There may be a variety of reasons for the simulated 10% O_3 reduction derived by the MECO(n) model for the O_3 profile on 28 May 2020. Uncertainties in the dynamics of the model, temporal or spatial shifts of patterns in the model compared to the observations, uncertainties in the emissions may contribute to this model result. A deeper analysis is required to better assess these deviations using more extensive model simulations as shown in the "Highlights from the BLUESKY mission" section.

Multiple Falcon and HALO flights were also performed in the industrial Po valley in Italy, a pollution hot spot in Europe, where pollution from large cities, e.g., Milan, are trapped in the river valley and by the Alps. As an example, Fig. 10 shows a Falcon measurement transect through the boundary layer in the western part of the Po valley between 46.6°N,

Brought to you by TU DELFT | Unauthenticated | Downloaded 11/07/22 01:10 PM UTC

9°E and 45°N, 10.4°E on 1 June 2020, covering the major industrial area of Milan. Measured CO volume mixing ratio are compared to HYSPLIT simulations interpolated to the Falcon flight path. The HYSPLIT simulations are based on the EDGAR emission inventory for CO of the Po valley region with business-as-usual emissions for the year 2017 adjusted to CO observations during the intense HALO measurements in the Italian Po valley during the Effect of Megacities on the transport and transformation of pollutants on the Regional to Global scales (EMERGE) campaign (Andrés Hernández et al. 2022). The observed CO mixing ratios in the major polluted areas during BLUESKY are lower by about 30% compared to the HYSPLIT simulations with no emission reductions for traffic and industry. The HYSPLIT trajectories enable a detailed allocation of emission inventory sources to the observed pollutant concentrations in the boundary layer. In future studies this will also comprise other pollutants such as nitrogen oxides with origins from several sectors. The example in Fig. 10 shows how concentrations of measured NO_y and HNO_3 vary by about one order of magnitude when descending from 2.5 to 1.2 km altitude. Still the HNO_3 relative fraction remains stable, as can be expected from rapid airmass exchange. This instrument performance allows the investigation of the propagation of (reduced) trace gas and aerosol emissions into the free troposphere.

Profiles of other anthropogenic and natural tracers. During BLUESKY, the I-CIMS and GC-MS instruments on board HALO measured two C3-organic nitrates: peroxypropionylnitrate, $CH_3CH_2C(O)OONO_2$, (PPN), and isopropylnitrate, $CH_3CH(ONO_2)CH_3$, (IPN). Both nitrates are formed during the OH-initiated oxidation of propane and are thus closely tied to anthropogenic emissions. PPN is formed subsequent to H-atom abstraction by OH from the CH_3 groups in propane and further oxidation. IPN is formed when the H abstraction takes place at the central C atom from the reaction of the isopropylperoxy radical with NO, albeit at low yield. The vertical profiles of PPN and IPN (Fig. 11, campaign average) indicate maximum values in the boundary layer, which reflects the fact that both are formed in the chemical degradation

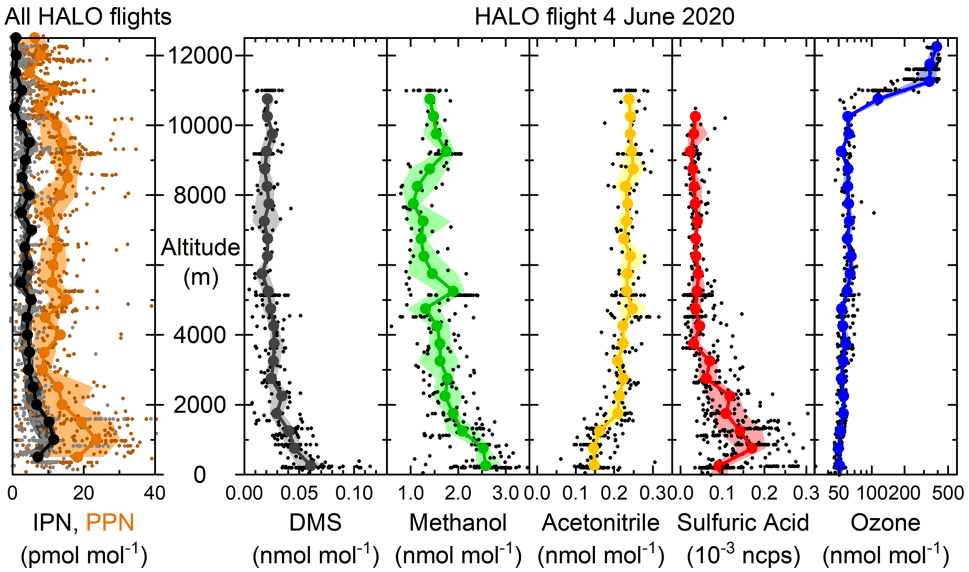


Fig. 11. (left) Vertical profiles of peroxypropionylnitrate [PPN; $CH_3CH_2C(O)OONO_2$] and isopropylnitrate [IPN; $CH_3CH(ONO_2)CH_3$] during all BLUESKY flights measured using the I-CIMS and the GC-MS instruments on HALO. (right) Vertical profiles measured on HALO on 4 Jun 2020 of dimethyl sulfide DMS, methanol, and acetonitrile measured by the GC-MS, gaseous sulfuric acid (H_2SO_4) measured by the CI-API-TOF, and O_3 measured by FAIRO. The flight path on 4 Jun 2020 covered southern Germany, France, Italy, and the Mediterranean. Dots represent individual measurements with 30 s time resolution for H_2SO_4 and O_3 and with 1 min resolution for the GC-MS data; solid lines represent data the median averaged to 500 m altitude bins and the shaded areas represent the corresponding quartiles. H_2SO_4 data are shown as normalized counts per second (NCPS).

Brought to you by TU DELFT | Unauthenticated | Downloaded 11/07/22 01:10 PM UTC

of propane emitted during anthropogenic activity at ground level. PPN has a broad, second maximum at around 8 km while IPN decreases quasi monotonically through the free and upper troposphere. The divergence in their vertical profiles can be understood in terms of their chemically different loss processes and different altitude dependent atmospheric lifetimes. PPN is thermally unstable at low altitudes, but reacts only slowly with OH so that its lifetime (mainly controlled by photolysis) is several months at the low temperatures of the upper troposphere. In contrast, IPN is stable with respect to both thermal decomposition and photolysis and is lost mainly by reaction with OH.

Also, organic compounds like acetonitrile and methanol and sulfur species like dimethylsulfide (DMS) were measured by the GC-MS and the PTR-Mass Spectrometer system on board HALO. Figure 11 in addition shows tropospheric concentrations of acetonitrile, methanol, and DMS for the HALO flight on 4 June 2020 over Germany, France, Italy, and the Mediterranean. Stratospheric data were separated and are treated separately in light of extensive ozone tests that were performed in the laboratory following BLUESKY. During HALO flight 6 (violet color in Fig. 6) the aircraft entered the marine boundary layer over the Mediterranean Sea and therefore DMS is enhanced at low altitudes caused by marine emissions of DMS, while acetonitrile is depleted as it is taken up at the sea surface. Methanol, a volatile organic compound of primarily biogenic origin, shows considerable structure caused by cloud outflow.

On the same flight, gaseous sulfuric acid was measured with the newly developed chemical ionization–atmospheric pressure interface time-of-flight mass spectrometer (CI-API-TOF) with a constant pressure inlet by reaction with nitrate ions. The inlet system was designed in a way to enable a high flow rate and to minimize sampling losses of nonvolatile compounds like sulfuric acid and highly oxygenated organic molecules. Low concentrations of gaseous H_2SO_4 were measured in the boundary layer and the free troposphere over central Europe. Here we show count rates respective for H_2SO_4 as the calibration of the pressure dependence of the mass spectrometer signal is ongoing. The data will be used to investigate the budget and the partitioning of the sulfur species, as also SO_2 and sulfate aerosol were measured on Falcon and HALO, respectively.

SO_2 was measured at cruise altitudes in the upper troposphere and lower stratosphere (UTLS) by the AIMS mass spectrometer on board the Falcon in order to investigate the contribution of anthropogenic and natural sources to the UTLS SO_2 budget. In 10–14 km altitude in the midlatitudes, SO_2 has a short life time of 13 ± 2 days (Höpfner et al. 2015). Figure 12 shows the

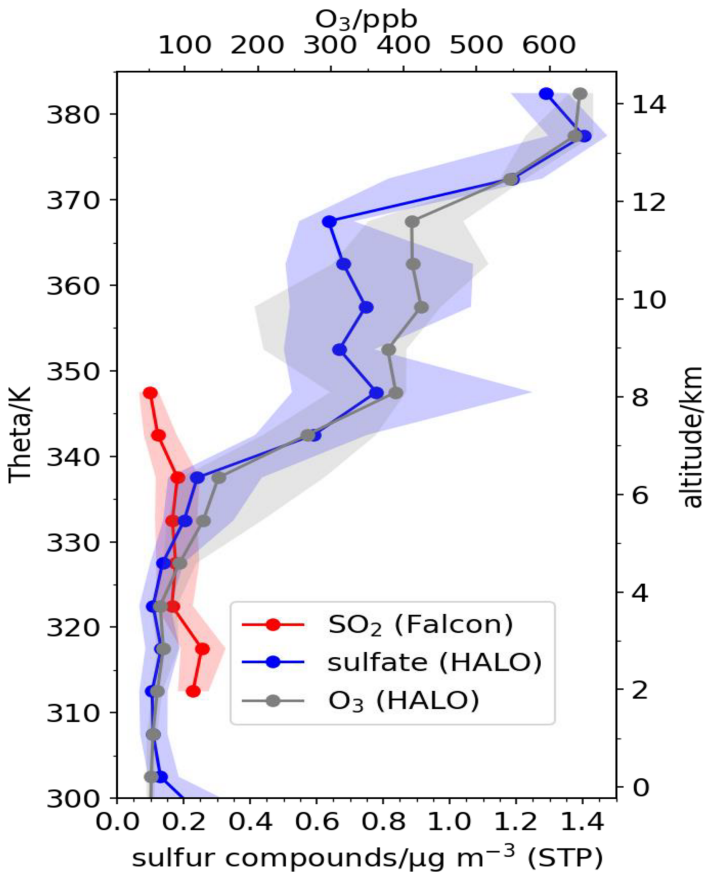


Fig. 12. Profiles of median SO_2 (red), sulfate (blue), and O_3 (gray) concentrations as well as quartiles (shaded) vs potential temperature. The data from all BLUESKY flights are plotted in 5 K bins. SO_2 was measured by AIMS on the Falcon, while sulfate and O_3 were measured on HALO.

Brought to you by TU DELFT | Unauthenticated | Downloaded 11/07/22 01:10 PM UTC

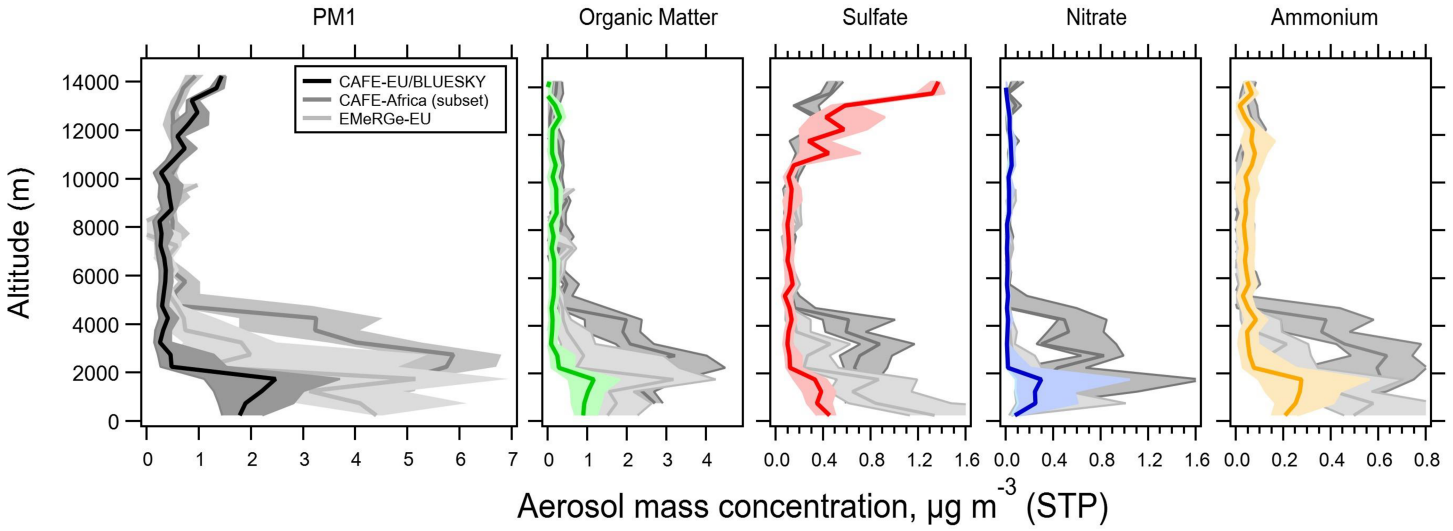


Fig. 13. Vertical profiles of total aerosol mass concentrations (including refractory black carbon) and aerosol mass concentrations of organics, sulfate, nitrate, and ammonium during BLUESKY (black and colors, medians and quartiles). Also shown are data from previous HALO missions over Europe: EMERGE-EU (light gray), conducted in July 2017 in the same area, and CAFE-Africa (gray), conducted between July and September 2018. From CAFE-Africa, only data measured in the same area as the other two missions were used (38°–57°N, 14°W–16°E).

median and quartiles of SO_2 profiles in the UTLS during the entire BLUESKY campaign for flight altitudes between 7.5 and 12.5 km. The maximum height is restricted by the Falcon flight altitude, while the lower limit is caused by a water vapor interference in the SO_2 measurement. The median SO_2 mixing ratio decreases with altitude from around 0.22 to 0.12 $\mu g\ m^{-3}$. SO_2 has been measured at similar altitudes above Europe in previous experiments: During the ITOP campaign in summer 2004, Speidel et al. (2007) reported 0.1 $\mu g\ m^{-3}$ SO_2 for high altitudes (<10.2 km) over Europe as confirmed by stratospheric background SO_2 measurements in August 2008 during CONCERT (Jurkat et al. 2010). Williamson et al. (2021) reported lower SO_2 concentrations over the Northern Hemispheric Pacific during the ATOM mission with values of 0.04 $\mu g\ m^{-3}$ in the upper troposphere and 0.07 $\mu g\ m^{-3}$ in the lower stratosphere. Overall, the BLUESKY SO_2 observations are in the upper range of reported background SO_2 concentrations in the continental UTLS. Nevertheless, the significant reductions in air traffic during the lockdown led to an SO_2 level lower than the 2008 background in aircraft flight corridors of 0.26 $\mu g\ m^{-3}$ (Jurkat et al. 2010). In the stratosphere, the SO_2 concentrations are much smaller than sulfate in aerosol, which is still enhanced from volcanic eruptions (see also Fig. 13).

Reductions of aerosol number concentration and aerosol mass in the troposphere. To study the possible influence of reduced ground and aircraft emissions during lockdown on aerosol mass concentrations, we compared the BLUESKY data to previous datasets obtained over Europe, namely, the EMERGE-EU campaign in July 2017 (Andrés Hernández et al. 2022) and the Chemistry of the Atmosphere–Field Experiment in Africa (CAFE-Africa) test and ferry flights conducted over Europe between July and August 2018. Figure 13 shows medians and quartiles of the parameters measured with the C-TOF-AMS on board HALO. For all four measured species, the concentrations measured in 2020 were lower, while in 2018 they were higher. For organics and sulfate, the EMERGE concentrations in 2017 were significantly higher than in 2020, while nitrate and ammonium show comparable values. Although the variability in the datasets is large, the consistent reductions indicated from the 2020 data for all four aerosol components suggests that they were at least partly due to diminished emissions during the lockdown. By combining our black carbon measurements with EMAC simulations we found a 40% reduction in black carbon mass related to the lockdown effects (Krüger et al. 2022).

Brought to you by TU DELFT | Unauthenticated | Downloaded 11/07/22 01:10 PM UTC

For organic aerosol mass, this finding holds also for the free troposphere above 5 km altitude, whereas for sulfate, nitrate, and ammonium the free-tropospheric data are comparable for all three datasets.

A recent model study using the EMAC model with reduced emission scenarios is able to reproduce the observations during the BLUESKY campaign (Reifenberg et al. 2022). Anthropogenic aerosol precursor gases include SO_2, NO_x, and VOCs. Although the emissions reductions had slightly leveled off in May and June compared to April 2020 (Guevara et al. 2021), still the NO_x reduction was highest with about 10%–20%, followed by SO_2 (9%–12%) and VOCs (2%–6%). Ammonia originates mainly from agriculture; therefore, no significant reduction was observed. However, the amount of NH_4 in the aerosol is determined by available acids (HNO_3 and H_2SO_4) to react with NH_3 to ammonium nitrate and sulfate. Direct $PM_{2.5}$ emissions were reduced only by 6%–9%. The finding that the observed differences in aerosol mass concentrations are much larger that the reduction in direct emissions suggests that secondary aerosol formation is the most important aerosol source over Europe. Below 2 km, sulfate and organics show a higher reduction compared to the previous campaigns than nitrate, indicating that the anthropogenic emissions of SO_2 and VOCs play a larger role for secondary aerosol formation than anthropogenic NO_x plays for secondary nitrate formation.

As discussed above, the strong increase of sulfate aerosol above 10 km and the higher sulfate mass concentrations observed in 2020 compared to 2018 may in part be due to the Raikoke volcanic eruption in June 2019 (Muser et al. 2020; de Leeuw et al. 2021), but also other, minor volcanic eruptions are likely to play a role.

Figure 14 shows profiles of fine mode aerosol number concentrations for particle sizes above 18 nm from the Falcon measurements during BLUESKY and the long-term observations from the In-service Aircraft for a Global Observing System–Civil Aircraft for the Regular Investigation of the Atmosphere Based on an Instrument Container (IAGOS-CARIBIC) project. The IAGOS-CARIBIC data shown here only include flights during the months May and June between 2005 and 2015. Profile data are restricted to central Europe between 8.8°W and 28°E and at latitudes between 40° and 66°N.

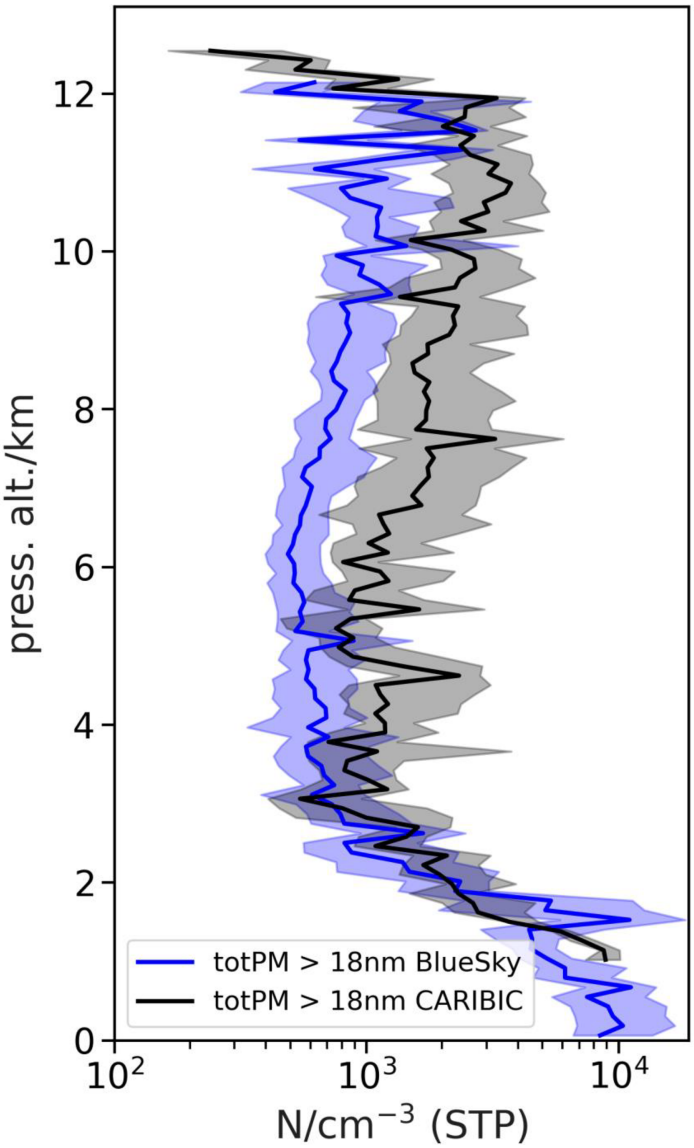


Fig. 14. Profiles of median and quartiles of aerosol number concentration (>18 nm) measured during BLUESKY (blue) in comparison to measurements performed by the CARIBIC-IAGOS project (black) during May and June between 2005 and 2015 in the same region (40°–66°N, 28°E–8.8°W).

Brought to you by TU DELFT | Unauthenticated | Downloaded 11/07/22 01:10 PM UTC

The median BLUESKY profile shows a clear reduction of the aerosol number concentration of 30%–70% in the free troposphere above 4 km altitude. At the tropopause above 11 km, the difference becomes less prominent, although the BLUESKY median concentrations are still mostly below the CARIBIC values, even though the IAGOS-CARIBIC data were measured 5– 15 years before BLUESKY with respective lower anthropogenic emissions. It is not possible to quantify an effect in the boundary layer although it has to be kept in mind that the BLUESKY flights represent a larger variety of low-level flights in different areas of Europe and the CARIBIC dataset is composed of primarily the ascents and descents into and out of Frankfurt international airport.

Blue sky during BLUESKY. The solar radiation at Earth's surface reached a maximum during the COVID-19 lockdown period in spring 2020 over western Europe. Van Heerwaarden et al. (2021) found that surface irradiance was highest since 1928 for the area of the Netherlands. Reasons were an overall very low cloud fraction, several exceptionally dry days, and low aerosol optical thickness (AOT). Regardless of whether AOT concentrations are ultimately due to an anthropogenic influence or related to meteorological variability, the subjective impression was that in 2020 the sky appeared in a deeper blue during the lockdown period. To substantiate this perception, we carried out radiative transfer calculations in the cloud-free atmosphere.

Simulations of the atmospheric radiative transfer are based on the 1D radiative transfer model UVSPEC from the program package libRadtran (Mayer and Kylling 2005; Emde et al. 2016). In this study, UVSPEC is used to compute downward-directed spectral radiances and irradiances at the surface in the visible spectral range (380–780 nm) for a cloud-free midlatitude summer standard atmosphere (Anderson et al. 1986). Regarding the aerosol, a model after Fenn et al. (1985) was used, which assumes a rural type for the boundary layer. To examine changes in sky color, calculated spectra are convolved with the spectral sensitivity of the human eye in the red, green, and blue spectral range. A subsequent spectral integration gives RGB color components and enables the representation of the sky color. Input to the model are different vertical distributions of the aerosol optical thickness AOT(z). Profiles close to reality have been generated by scaling a normalized profile of the volume extinction coefficient (Fenn et al. 1985) with a total AOT provided by the Moderate Resolution Imaging Spectroradiometer (MODIS) on board the *Terra* and *Aqua* satellites.

The total aerosol optical thicknesses derived from MODIS data products MOD08_D3 v6.1 (*Terra*) and MYD08_D3 v6.1 (*Aqua*) were statistically analyzed over Germany and Europe. Here we consider the BLUESKY period from 23 May to 9 June 2020 as a reference to the years 2015–19. For 2020 the median total aerosol optical thickness $\mathrm{AOT}_{\mathrm{MODIS}}$ is 0.156 at 0.55 μm, whereas it is 0.247 for the period 2015–19. For comparison, the individual years 2015–19 give an $\mathrm{AOT}_{\mathrm{MODIS}}$ range between 0.187 and 0.309. Also, the statistics for Europe shows a median of 0.156 for the BLUESKY period in 2020 and a range of 0.175 to 0.265 for 2015–19. Vertical profiles of the aerosol optical thickness based on the $\mathrm{AOT}_{\mathrm{MODIS}}$ values of 0.156 and 0.247 are presented in Fig. 15a. Figure 15b shows the spectra of the diffuse component of downward directed spectral irradiances for a solar zenith angle of 45°. Calculating the ratio r of downward irradiances at blue and red wavelengths ($I_{460\mathrm{nm}}/I_{750\mathrm{nm}}$), for example, results in $r = 2.4$ and $r = 2.1$ for $\mathrm{AOT}_{\mathrm{MODIS}}$ of 0.156 and 0.247, respectively, indicating a shift of the simulated spectrum toward shorter wavelengths. Figures 15c and 15d reveal that the spectra are associated with a contrast in sky color. Transferring angular resolved radiances and hemispherically integrated irradiances into RGB colors clearly illustrates that in case of a reduced $\mathrm{AOT}_{\mathrm{MODIS}}$ (Figs. 15c and 15d, left halves of circles), the sky appears in a deeper blue color. This result also applies to other solar zenith angles. Figure 15e displays the year-to-year variability of the $\mathrm{AOT}_{\mathrm{MODIS}}$ in the period from 2015 to 2020 highlighted with calculated sky colors. It is obvious that the blue

Brought to you by TU DELFT | Unauthenticated | Downloaded 11/07/22 01:10 PM UTC

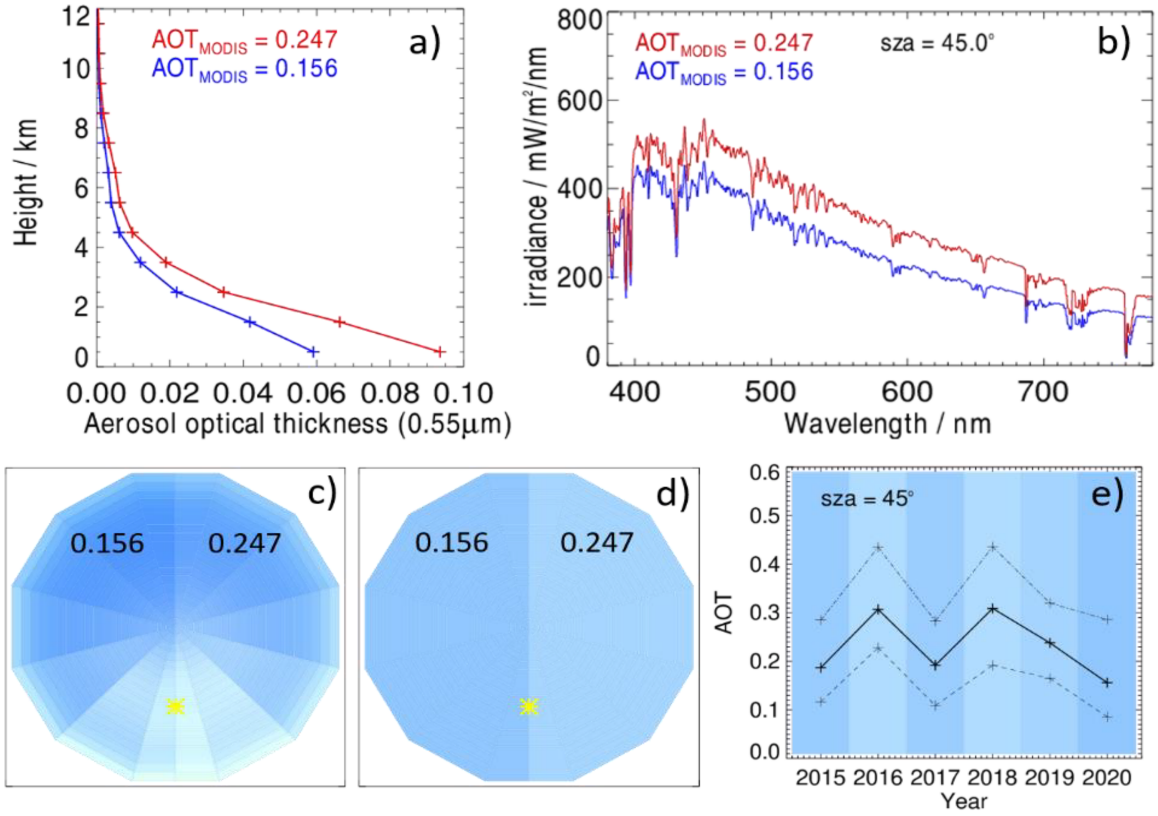


Fig. 15. Blue sky during BLUESKY. (a) Vertical profiles of the aerosol optical thickness at 550 nm scaled to different medians of the total aerosol optical thicknesses AOT$_{MODIS}$ derived from MODIS data covering the area of Germany. Blue: scaled with the median valid for the BLUESKY period in 2020; red: scaled with the median resulting from all BLUESKY periods of the years 2015–19. (b) Spectral distributions of the diffuse component of the downward directed irradiance at the surface for the AOT$_{MODIS}$ as in (a). SZA denotes the solar zenith angle data. (c) Sky colors derived from calculated spectral radiances integrated over the visible spectral range (380–780 nm) convolved with the spectral sensitivity of the human eye. Radiance distributions are displayed relative to the position of the sun (yellow star). Left and right halves of the circles represent colors resulting for AOT$_{MODIS}$ values as indicated. At the center of each circle the viewing zenith angle is 0°. (d) As in (c), but for downward-directed irradiances resulting from an angular integration of the radiances shown in (c) over the upper hemisphere. (e) Year-to-year variability of AOT$_{MODIS}$ for the area of Germany in the period from 2015 to 2020. Dashed and dashed–dotted curves represent minima and maxima of the AOT$_{MODIS}$ within the BLUESKY period of each year.

in 2020 forms a contrast to all previous years, albeit differently pronounced depending on the AOT$_{MODIS}$ differences. Although it is not clear whether changes in the total aerosol optical thickness are mainly due to an anthropogenic or a meteorological influence, the radiative transfer simulations give a clear indication that the lower aerosol optical thickness during the lockdown resulted in a deeper blue color of the sky during BLUESKY compared to the same period in the previous five years. Global model simulations in the "Highlights from the BLUESKY mission" section further investigate the impact of aerosol changes on the radiation budget at the surface.

Effect of pollution on low clouds. To contrast aerosol–cloud interactions in highly polluted regimes against less polluted regimes, intensive measurements of aerosol and clouds were made in the boundary layer over the densely populated Ruhr metropolitan region versus recurrent sampling of the boundary layer over the remote sparsely populated Hohenpeissenberg regions in southern Germany. Further aerosol and cloud measurements were taken above the cities of Berlin, Hamburg, and Munich, during individual arrival and departure routes to and from the respective airports.

Brought to you by TU DELFT | Unauthenticated | Downloaded 11/07/22 01:10 PM UTC

Cloud droplet number concentrations (CDNC) in low-level clouds (<2,500 m altitude) were measured with the Cloud and Aerosol Spectrometer (CAS) probe aboard the DLR Falcon and more than 8,000 individual clouds were intercepted. We implemented a cloud threshold considering only droplets larger than 3 μm and with a liquid water content of more than 0.01g m^{-3}, in order to avoid diffuse cloud edges. Only measurements contributed to the remote Hohenpeissenberg statistics from campaign days without a large-scale westerly flow, to avoid an influence of the Munich urban emission plume. Figure 16 shows the cloud droplet number concentrations measured in the remote and the industrial regions. A clear trend is observed between the CDNC in the rural Hohenpeissenberg area with median cloud drop number concentrations of a few tens per cubic centimeters at the lower side of the spectrum and high median CDNC of 385 cm^{-3} in the densely populated Ruhr metropolitan area. The cities of Hamburg (195 cm^{-3}), Berlin (274 cm^{-3}), and Munich (311 cm^{-3}) range in between.

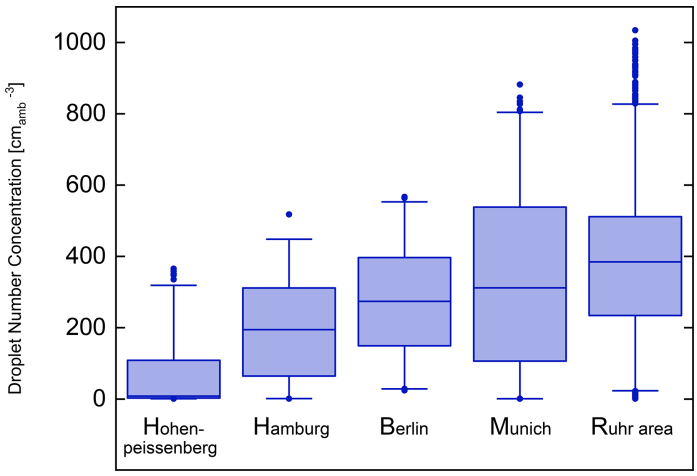


Fig. 16. Statistics of cloud droplet number concentrations (CDNC) in low-level clouds in rural, urban, and industrial regions of Germany during the BLUESKY campaign measured with the CAS on board the Falcon. The figure shows the medians, quartiles, and 1% and 99% percentiles of all cloud intercepts in the different regions. The trend in CDNC number concentration correlates with pollution levels, with lowest CDND in the remote Bavarian Hohenpeissenberg region [number of cloud intercepts (*n*) = 616], intermediate CDNC related to city outflow from Hamburg (*n* = 152), Berlin (*n* = 330), and Munich (*n* = 608) and highest CDNC in the industrial Rhine–Ruhr metropolitan area (*n* = 4,751).

Reduced contrail cirrus cover and radiative impact. The COCIP (Schumann 2012) simulates the life cycle of contrails (Schumann et al. 2017; Schumann and Heymsfield 2017) that form for given aircraft flight track data and numerical weather predictions and computes their local radiative forcing (Schumann 2012). COCIP has been used for mission planning, for simulation of contrail properties comparable with in situ and satellite observations, and for aviation climate impact mitigation studies (Schumann and Graf 2013; Voigt et al. 2017; Teoh et al. 2020; Schumann et al. 2021a). Figure 17 presents example results for 16 April 2020. Travel restrictions in response to COVID-19 caused an 89% decrease in air traffic flight distance over Europe this day. Despite the low air traffic density, MSG/SEVIRI data indicate contrail occurrence on that day, as shown in the optical thickness of ice clouds, derived using the algorithm described in Strandgren et al. (2017), and from brightness temperature differences.

Contrail and cirrus optical thickness (COT) derived from COCIP on that day are shown in the middle panel in Fig. 17, as well as COCIP COT calculated with the same meteorology but with air traffic data from 16 April 2019. Higher contrail cirrus optical thickness is calculated for the factor-of-5-higher air traffic on 16 April 2019. COCIP was also used to calculate the respective positive and negative radiative forcing (RF) from contrail cirrus for both scenarios. The resulting daily net forcing is positive on average in both years. The computed longwave and shortwave RF components locally exceed 1 W m^{-2} in magnitude despite low air traffic in 2020. On 16 April 2020, the contrail RF in the presented area is also strongly reduced to about 20% of its value for the same meteorology but for air traffic data in 2019, implying a significant reduction in RF from contrails due to reduced air traffic in 2020 on that day.

Brought to you by TU DELFT | Unauthenticated | Downloaded 11/07/22 01:10 PM UTC

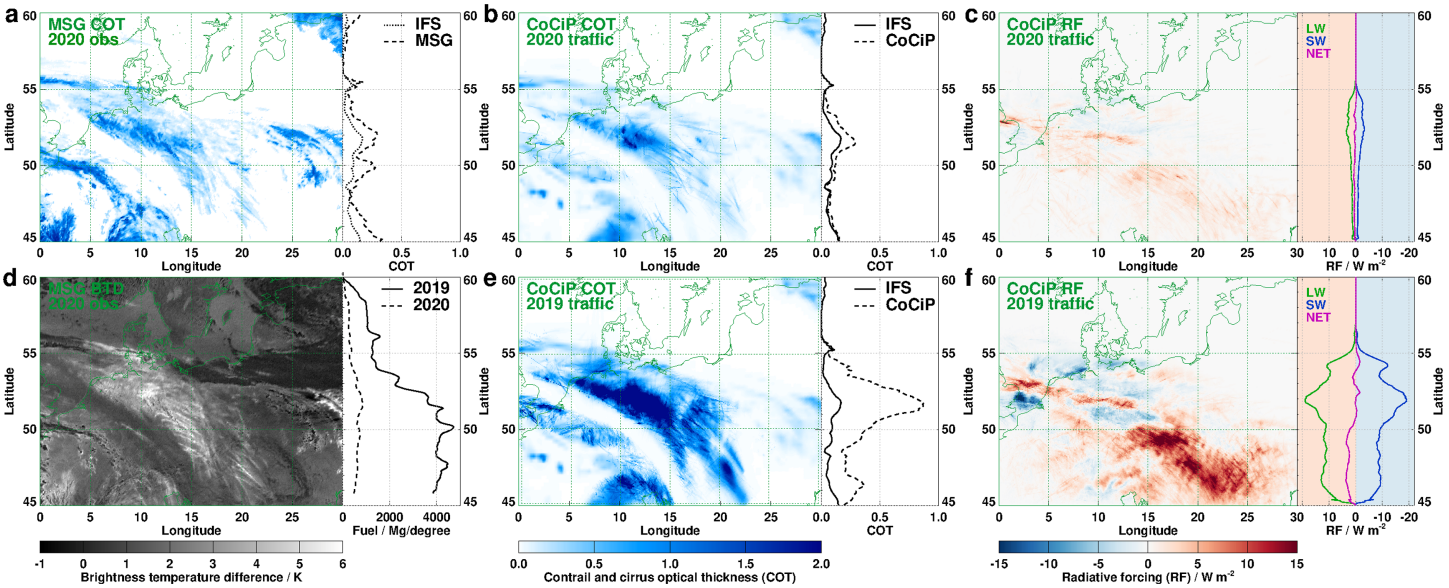


Fig. 17. Cirrus optical thickness derived from (a) MSG/SEVIRI satellite observations and contrail cirrus optical thickness modeled with COCIP for 1000 UTC 16 April 2020 (b) for air traffic of 2020 and (e) for air traffic of 2019, and (d) brightness temperature difference between 10.8 and 12.0 μm channels of MSG/SEVIRI, with color bars. Please notice that all COT plots use the same white–blue color scale depicted below (e). The line diagrams show longitudinal averages of the optical thickness in (a), (b), and (e), and of derived aircraft fuel consumption in (d). The cirrus optical thicknesses are derived from observations (MSG, dashed lines), from ECMWF-IFS numerical weather predictions (IFS, dotted), and from the combined IFS and COCIP model (COCIP, full). The diurnal fuel consumption per degree latitude is derived from EUROCONTROL traffic data (CPR) for 16 April 2019 (full line) and 2020 (dashed). (c),(f) The radiative forcing from contrail cirrus in 2020 and the expected forcing for air traffic in 2019 calculated with COCIP.

Annually averaged changes might be different due to the warming and cooling components of the contrail cirrus forcing (Gettelman et al. 2021). A more detailed discussion of the contrail effects including an uncertainty analysis is given in Schumann et al. (2021a) and the extension to longer time periods is discussed in Schumann et al. (2021b).

Changes in cirrus properties from* CALIPSO *data. Civil aviation may contribute to climate change by inducing contrail cirrus formation and by changing natural cirrus cloud properties (Tesche et al. 2016). Urbanek et al. (2018) showed that cirrus clouds formed in regions highly affected by air traffic have higher mean particle linear depolarization ratios than those formed in pristine regions. To study the effect of reduced aviation on cirrus cloud properties we compared *CALIPSO* satellite measurements of cirrus during the BLUESKY campaign with cirrus data measured at the same time period in the previous years (2010–19). The measurements were performed with CALIOP instrument on board the *CALIPSO* satellite (Winker et al. 2007, 2010; Stephens et al. 2018). CALIOP uses three channels at 1,064 and 532 nm for measuring the total backscatter and the orthogonal component of depolarization. For this study we used the level 2 5 km cloud profile products with a vertical resolution of up to 30 m. To compare the CALIOP cirrus observations with the measurements during the BLUESKY campaign, we analyzed the datasets covering the Falcon cruise area from 50° to 55°N and from 15°W to 5°E as well as latitudes from 45° to 55°N and longitudes from 5° to 15°E. *CALIPSO* passes over the study area three to four times each day resulting in 90 overpasses in the period 16 May–9 June each year. Since all BLUESKY measurements were performed during the day, we only used daytime satellite lidar observations for the intercomparison.

To investigate the changes of cirrus cloud properties as possible consequence of the significantly reduced aviation during the COVID-19 pandemic, we used the particle linear depolarization ratio (PLDR), the extinction coefficients (σ_{ci}), and the calculated effective optical thickness of cirrus clouds ($\tau_{ci} = \int_{r_b}^{r_t} \sigma_{ci}\, dz$, where r_t and r_b are the cloud-top and

Brought to you by TU DELFT | Unauthenticated | Downloaded 11/07/22 01:10 PM UTC

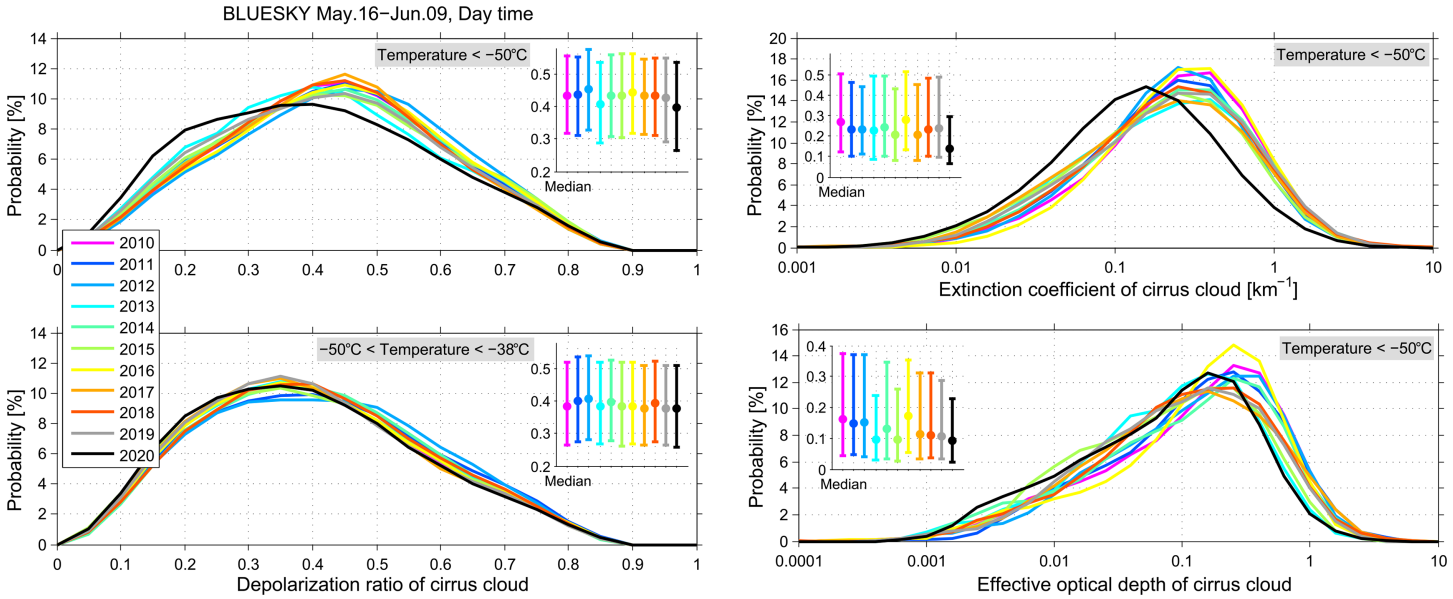


Fig. 18. Comparisons of cirrus cloud properties determined from the lidar measurements of *CALIPSO* in the years 2010–20 over Europe in the period from 16 May to 9 Jun 2020 during BLUESKY. (left) Particle linear depolarization ratios (PLDR) of cirrus clouds determined from the daytime observations at temperatures (top left) below –50°C and (bottom left) between –50°C and –38°C; (top right) extinction coefficient (σ_{ci}) in the cirrus clouds at temperatures colder than –50°C and (bottom right) effective cloud optical depth of cirrus ($\tau_{e,ci}$) at temperatures lower than –50°C. The medians (circles) of PLDR, σ_{ci}, and $\tau_{e,ci}$ of cirrus clouds as well as the quartiles (lower and upper bars, respectively) in years 2010–20 are indicated in the inserted boxes.

cloud-bottom heights of cirrus, respectively). As cirrus cloud properties strongly depend on temperatures (e.g., Urbanek et al. 2018), and as a temperature T of –50°C is one of the threshold conditions for contrail formation (Schumann 1996), we divided the data into two subsets with temperatures from –38° to –50°C and temperatures below –50°C (Li and Groß 2021).

Figure 18 shows the probability density function (PDF) of the PLDR (left) for cirrus clouds at T < –50°C (top panel) and –50° < T < –38°C (bottom panel), as well as of the extinction coefficient (top right) and the effective optical depth (bottom right) for T < –50°C of all cirrus cloud cases measured during the day with CALIOP during the BLUESKY period in the different years. The resulting distributions of cirrus PLDR show a non-Gaussian shape for both temperature ranges with larger values at the lower temperature range (T < –50°C). The PDFs of the PLDR of cirrus clouds in the higher temperature range show almost no deviation from each other, and also the cirrus cloud measurements in 2020 are well within the variability of the previous years. The median of the PLDR distribution is at about 0.35–0.38 for all the years. For the cirrus PLDR at the lower temperature range, the situation looks quite different. The years 2010–19 show only limited variability with a median value between 0.42 and 0.45. However, the PLDR for the cirrus clouds measured during BLUESKY in 2020 show a significantly lower median value of 0.39. The σ_{ci} and τ_{ci} distributions show the same features as PLDR; σ_{ci} and τ_{ci} values for cirrus clouds in 2020 are on average smaller at lower temperatures than in the previous years. The median value of the extinction coefficient for the years 2010–19 varied between 0.20 and 0.26 km^{-1} while it was about 0.14 in 2020. A similar but not as significant picture is found for the cirrus cloud effective optical thickness. Most median values in the years 2010–19 were within a range of 0.10 and 0.16, whereas the median value in 2020 was about 0.09. Low values are, however, also found for cirrus clouds in 2013 and 2015.

Global chemistry–climate modeling. The input and the comparison of measurement data with global models are essential to enhance our understanding of atmospheric processes and their relation to climate. The EMAC atmospheric chemistry–climate model was used

Brought to you by TU DELFT | Unauthenticated | Downloaded 11/07/22 01:10 PM UTC

both for forecasting and the postcampaign data analysis. In both cases EMAC was nudged by Newtonian relaxation toward data from the European Centre for Medium-Range Weather Forecasts (ECMWF). The EMAC atmospheric model core is the fifth-generation European Centre Hamburg general circulation model (ECHAM5). For higher resolution in the field campaign region, the forecasts of atmospheric composition were performed with the MECO(n) model, which couples the global EMAC model online with the enhanced resolution regional model COSMO/MESSy, allowing for seamless zooming into regions of interest in the global model context (Kerkweg and Jöckel 2012a,b; Mertens et al. 2016). A continuous analysis simulation is performed from which 5-day forecasts are branched of every 12 h, with nudging toward the ECMWF operational analysis/forecast data. MECO(n) was configured with one refinement ranging from eastern North America to eastern Europe with 0.44° resolution in latitude and longitude. Comprehensive tropospheric gas phase chemistry was calculated as described by Mertens et al. (2016), in addition the source apportionment method by Grewe et al. (2017) and Mertens et al. (2020) was applied. Here, it uses a business as usual air traffic scenario to help identify the regions where large aviation signals onto the NO_y mixing ratios are predicted.

As an example, Fig. 19 shows the NO_y mixing ratios at 250 hPa averaged for 0700–1600 UTC 2 June 2020 and the relative contribution of aviation nitrogen oxide emissions to the NO_y mixing ratios. The model forecast shows regions with relative contributions from air traffic of more than 50% predicted west of Ireland for a business as usual air traffic scenario. The predictions were used to guide both aircraft into regions with aircraft emissions for aviation in 2019, being reduced during the same period in 2020. Accordingly, HALO and Falcon performed measurement flights in the regions west of Ireland (Fig. 19). The NO_x and NO_y measurements on the HALO and the Falcon during their flights into this area show individual spikes in NO_x and NO_y indicating the presence of a few aircraft plumes. In addition, NO_x and NO_y plumes from aircraft flying on 2 June 2020 as well as for air traffic in 2019 were calculated with the COCIP model and folded onto the Falcon and HALO flight paths. Due to reduced air traffic in 2020 only few individual plumes are derived, while calculations for emissions from the denser air traffic in 2019 show many more spikes.

Postcampaign data analysis was also performed with the EMAC model, adopting reduced emissions resulting from the lockdown in Europe as estimated by Guevara et al. (2021). EMAC was nudged toward the ERA-Interim data (Berrisford et al. 2011) to reproduce the observed synoptic weather conditions.

Figure 20 shows a comparison of observed temperature, specific humidity, CO, NO, O_3, and photolysis frequencies $j(NO_2)$ from HALO measurements and EMAC results from simulations with the reduced emission (COVID-19) scenario (Reifenberg et al. 2022). The good agreement between observed and simulated data for temperature, which is a nudged variable and therefore shows the same variance as the ERA-Interim dataset, indicates the quality of the reproduced meteorology. As expected, somewhat larger deviations from the observations are found for unconstrained variables, such as O_3, CO, and NO, although the overall comparison shows a very good agreement of the low-emission scenario simulations with the HALO measurements. In particular, the model is able to reproduce the observed NO, which was strongly reduced in the entire tropospheric column, because of the strong reductions in ground and air traffic (e.g., Schumann et al. 2021a). Furthermore, also parameters which are strongly influenced by parameterizations are satisfactorily represented in the model, such as the photolysis frequency of $j(NO_2)$, whose variability is associated with clouds. In addition, O_3 is in general agreement between model and observations, albeit with modeled O_3 concentrations tending to slightly higher values. The EMAC model has also been used to investigate the impact of reduced emissions on direct and indirect aerosol radiative forcing during COVID-19 lockdown in Europe. Reifenberg et al. (2022) find large differences of selected tracers and aerosol between the reduced emission (COVID-19) scenario and the business as usual scenario at aircraft cruise altitudes in the upper troposphere mainly

Brought to you by TU DELFT | Unauthenticated | Downloaded 11/07/22 01:10 PM UTC

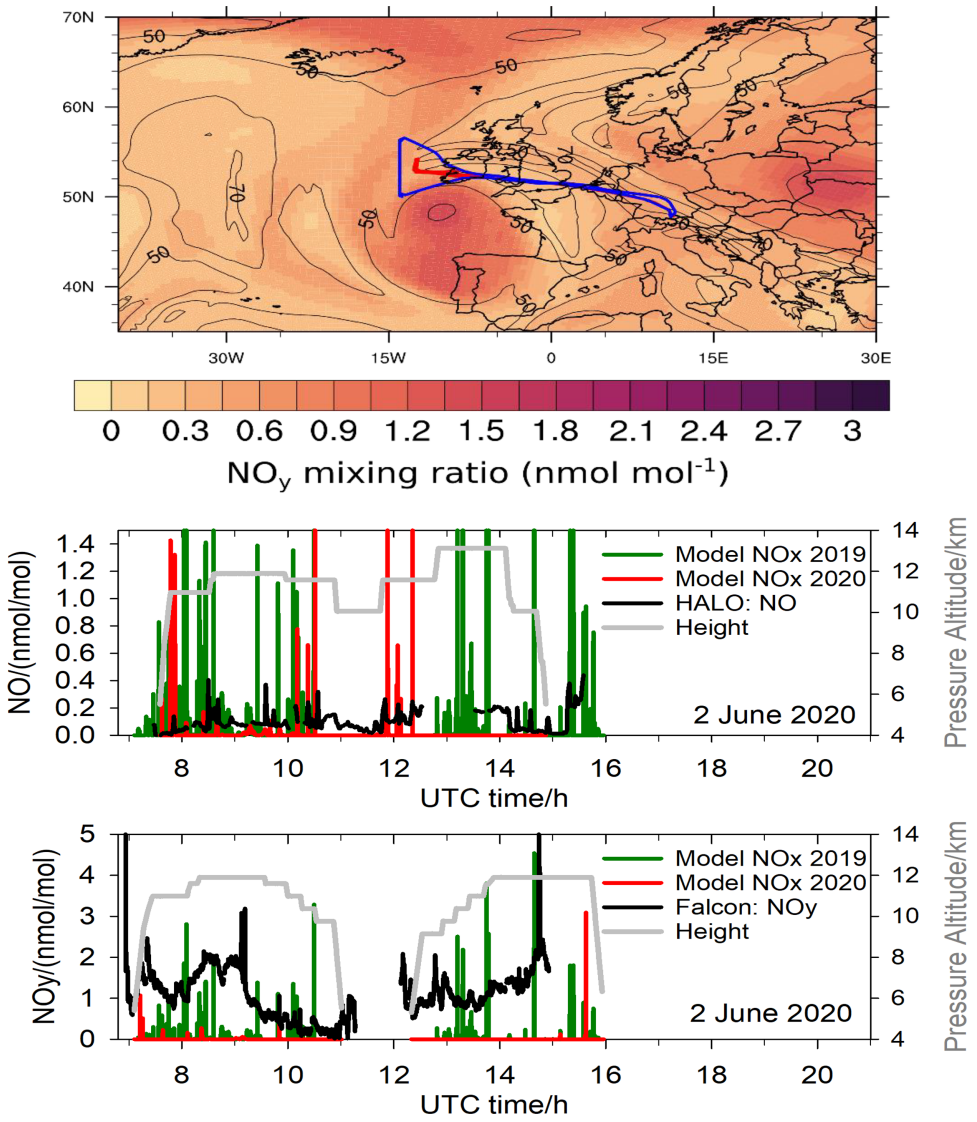


Fig. 19. (top) NO_y mixing ratios (in nmol mol^{-1}) at 250 hPa over Europe averaged from 0700 to 1600 UTC 2 Jun 2020. The black contours show the relative contribution (in %) of aviation emissions to the NO_y mixing ratios for the business as usual scenario using the tagging attribution method. The blue line shows the flight path of HALO, and the red line shows the flight path of the Falcon. The predictions were used to guide the aircraft into regions with expected reduced aircraft emissions. (middle),(bottom) The NO and NO_y data measured on that day by HALO and Falcon, respectively. Individual spikes in NO and NO_y indicate aircraft plumes. The red (green) lines show COCIP contrail model plume NO_x emitted by aircraft on that day in 2020 (red) and on the same day in 2019 (green) folded onto the Falcon and HALO flight paths. The number of plume observations agrees better with the 2020 aircraft scenario.

due to reduced air traffic. In addition, noticeable differences are found in the boundary layer affected mainly by ground transportation and industry. The reduction in aerosol surfaces leads to an increase in incoming solar radiation at the surface during the BLUESKY period (Reifenberg et al. 2022), in addition to the blue sky color.

Conclusions and outlook

From 16 May to 9 June 2020 the HALO and DLR Falcon performed 20 flights over Europe during the early COVID-19 lockdown to investigate the impact of reduced anthropogenic emission on the atmospheric composition during the BLUESKY mission. A comprehensive and unique dataset of trace gases, aerosols, and clouds was measured from the boundary layer to the lower stratosphere and profiles of atmospheric constituents were derived and compared to

Brought to you by TU DELFT | Unauthenticated | Downloaded 11/07/22 01:10 PM UTC

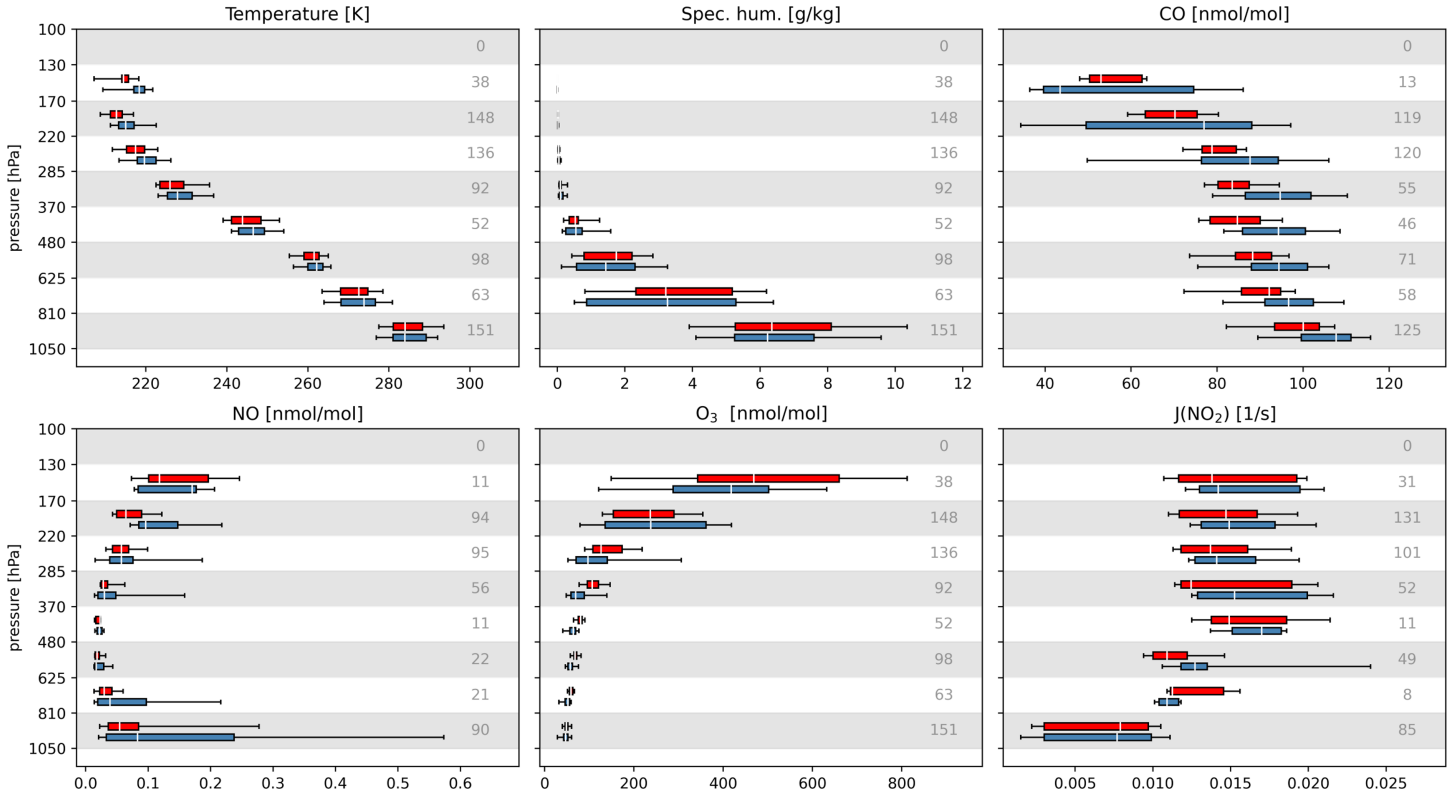


Fig. 20. Vertical distribution of EMAC model results with a reduced emission scenario (red) and BLUESKY aircraft measurements (blue) of trace species and the meteorological variables (temperature and specific humidity), represented by box-and-whisker plots for pressure bins (Reifenberg et al. 2022). The white line marks the median, the box corresponds to lower and upper quartiles, and the whiskers represent the 5th and 95th percentiles. The gray numbers on the right indicate the number of observed and interpolated simulated data points for each pressure bin. Measurements were averaged over 5 min periods to match the time resolution of the model.

measurements in pre-COVID-19 times and to satellite data and models. This paper presents first highlights from BLUESKY:

1) Significant (10%–50%) tropospheric NO_2 reductions were observed over industrialized continental areas as well as in major city outflows during the early lockdown phase, indicated by TROPOMI and GOME satellite data.
2) Tropospheric NO_y and CO profiles over Frankfurt showed significant (20%–70%) reductions on 28 May 2020 compared to the MOZAIC climatology from 2004 to 2015 and to IAGOS measurements from 2016 to 2019. The measured PPN and IPN profiles are in line with reduced anthropogenic influence on atmospheric chemistry. Falcon measurements of CO and NO_y in the industrial boundary layer of the Po valley in Italy show reductions up to 30%.

   EMAC model results confirm the impact of reduced emissions on the NO_y and CO profiles over Frankfurt. A comparison of EMAC results to BLUESKY O_3 data suggests that tropospheric O_3 is in general agreement with the observations, but tends to be slightly elevated compared to the HALO observations during the lockdown phase in Europe.
3) A suite of sulfur species was measured, such as DMS, SO_2, and H_2SO_4 as well as sulfate aerosol, which makes it possible to investigate the sulfur budget in the UTLS. The stratospheric sulfate was still perturbed by the aged emissions from the volcanic Raikoke eruption in June 2019 and by smaller eruptions thereafter.
4) The aerosol fine mode number concentrations and mass were substantially reduced in continental profiles with respect to observations from previous European summer campaigns and from the MOZAIC dataset. In the lower troposphere blow 5 km, we found strong aerosol

Brought to you by TU DELFT | Unauthenticated | Downloaded 11/07/22 01:10 PM UTC

mass reductions. For black carbon aerosol, the lockdown-related reduction was as high as 40% (Krüger et al. 2022). Reduced organic aerosol particulates aloft imply that reduced VOC emissions transported from the surface might have led to a reduction of secondary organic aerosol production in the free troposphere.

5) The perceived deeper blue sky during the BLUESKY period in central Europe can be explained by reduced light scattering from aerosol profiles with a 40% lower AOT than usual.
6) Low-level clouds measured in remote parts of Bavaria contained lower cloud droplet number concentrations compared to clouds over large cities and the industrial Ruhr region.
7) The 80% reduced air traffic led to significant reductions in contrail cover, contrail optical thickness and to a reduced, but still positive radiative forcing from contrail cirrus for a case study relating to 16 April 2020. Also, observed reductions in NO_y at cruise altitudes can be explained by simulated reductions in aircraft NO_x emissions.
8) The extinction and the depolarization ratio of cirrus clouds below −50°C measured by CALIOP on daytime between 16 May and 9 June 2020 exhibits reductions at aircraft cruise altitudes above Europe implying a potential effect from reduced aircraft aerosol emissions on cirrus properties.
9) The global model EMAC has been used in its nudged version for flight planning. First postcampaign simulation results indicate good agreement for a scenario with emissions that were reduced during the lockdown period. Reifenberg et al. (2022) derive a higher fraction of incoming solar radiation at the surface for the reduced COVID-19 emission scenario compared to the business as usual simulations, mainly due to reduced aerosol surface areas.

Altogether, BLUESKY provides a comprehensive dataset on trace gases, aerosols, and clouds over Europe, which documents the anthropogenic impact on atmospheric composition and climate.

Acknowledgments. We thank the DLR flight department for support during the campaign and the pilots for excellent flight operations. Support by the Helmholtz Association, the Max-Planck-Society, and by the German Science Foundation DFG within the SPP HALO 1294 under Grants VO1504/5-1, VO1504/7-1, BO1580/5-1, and of the CRC TRR 301/1 TP Change is acknowledged. Also support by the Dr. Hans Messer Foundation and the Heinrich Böll Stiftung is acknowledged. *Sentinel-5P* is a European Space Agency (ESA) mission on behalf of the European Commission (EC). Special thanks to Markus Hermann and Denise Assmann (TROPOS) for providing IAGOS-CARIBIC particle data for aerosol concentration comparisons (www.iagos.org/iagos-caribic). MetOp/GOME-2 level 2 data are provided by DLR in the framework of the EUMETSAT AC-SAF project. The EMAC and MECO(n) simulations have been performed at the German Climate Computing Centre (DKRZ) through support from the Bundesministerium für Bildung und Forschung (BMBF). DKRZ and its scientific steering committee are gratefully acknowledged for providing the HPC and data archiving resources for the project "Multiscale Earth System Chemistry Modelling." The authors thank the NASA Langley Research ASDC and *CALIPSO* science team for making the data available for research.

Data availability statement. Data are available on request at the HALO database at https://halo-db.pa.op.dlr.de/mission/119. The *Sentinel-5P*/TROPOMI level 2 data are freely available via the Copernicus Open Access Hub (https://s5phub.copernicus.eu/).

Brought to you by TU DELFT | Unauthenticated | Downloaded 11/07/22 01:10 PM UTC

References

Anderson, G. P., S. A. Clough, F. X. Kneizys, J. H. Chetwynd, and E. P. Shettle, 1986: AFGL atmospheric constituent profiles (0–120 km). Air Force Geophysics Lab Tech. Rep. AFGL-TR-860110, 43 pp.

Andreae, M. O., and Coauthors, 2018: Aerosol characteristics and particle production in the upper troposphere over the Amazon basin. *Atmos. Chem. Phys.*, **18**, 921–961, https://doi.org/10.5194/acp-18-921-2018.

Andrés Hernández, M. D., and Coauthors, 2022: Overview: On the transport and transformation of pollutants in the outflow of major population centres—Observational data from the EMeRGe European intensive operational period in summer 2017. *Atmos. Chem. Phys.*, **22**, 5877–5924, https://doi.org/10.5194/acp-22-5877-2022.

Baumgardner, D., G. Kok, and G. Raga, 2004: Warming of the Arctic lower stratosphere by light absorbing particles. *Geophys. Res. Lett.*, **31**, L06117, https://doi.org/10.1029/2003GL018883.

Bekbulat, B., J. Apte, D. Millet, A. Robinson, K. Wells, and J. Marshall, 2020: $PM_{2.5}$ and ozone air pollution levels have not dropped consistently across the US following societal COVID response. ChemRxiv, https://doi.org/10.26434/chemrxiv.12275603.v2.

Berrisford, P., and Coauthors, 2011: The ERA-Interim archive, version 2.0. ERA Rep. Series 1, 23 pp., www.ecmwf.int/sites/default/files/elibrary/2011/8174-era-interim-archive-version-20.pdf.

Bohn, B., and I. Lohse, 2017: Calibration and evaluation of CCD spectroradiometers for ground-based and airborne measurements of spectral actinic flux densities. *Atmos. Meas. Tech.*, **10**, 3151–3174, https://doi.org/10.5194/amt-10-3151-2017.

Bourtsoukidis, E., F. Helleis, L. Tomsche, H. Fischer, R. Hofmann, J. Lelieveld, and J. Williams, 2017: An aircraft gas chromatograph-mass spectrometer System for Organic Fast Identification Analysis (SOFIA): Design, performance and a case study of Asian monsoon pollution outflow. *Atmos. Meas. Tech.*, **10**, 5089–5105, https://doi.org/10.5194/amt-10-5089-2017.

Bräuer, T., and Coauthors, 2021a: Airborne measurements of contrail ice properties—Dependence on temperature and humidity. *Geophys. Res. Lett.*, **48**, e2020GL092166, https://doi.org/10.1029/2020GL092166.

——, and Coauthors, 2021b: Reduced ice number concentrations in contrails from low-aromatic biofuel blends. *Atmos. Chem. Phys.*, **21**, 16817–16826, https://doi.org/10.5194/acp-21-16817-2021.

Burkhardt, U., L. Bock, and A. Bier, 2018: Mitigating the contrail cirrus climate impact by reducing aircraft soot number emissions. *npj Climate Atmos. Sci.*, **1**, 37, https://doi.org/10.1038/s41612-018-0046-4.

Chen, L. A., L. C. Chien, Y. Li, and G. Lin, 2020: Nonuniform impacts of COVID-19 lockdown on air quality over the United States. *Sci. Total Environ.*, **745**, 141105, https://doi.org/10.1016/j.scitotenv.2020.141105.

Clark, H., and Coauthors, 2021: The effects of the COVID-19 lockdowns on the composition of the troposphere as seen by In-service Aircraft for a Global Observing System (IAGOS) at Frankfurt. *Atmos. Chem. Phys.*, **21**, 16237–16256, https://doi.org/10.5194/acp-21-16237-2021.

Copernicus, 2020: Emissions changes due to lockdown measures during the first wave of the COVID-19 pandemic in Europe. Accessed 30 September 2021, https://atmosphere.copernicus.eu/emissions-changes-due-lockdown-measures-during-first-wave-COVID-19-pandemic-europe.

de Leeuw, J., and Coauthors, 2021: The 2019 Raikoke volcanic eruption—Part 1: Dispersion model simulations and satellite retrievals of volcanic sulfur dioxide. *Atmos. Chem. Phys.*, **21**, 10851–10879, https://doi.org/10.5194/acp-21-10851-2021.

Derstroff, B., and Coauthors, 2017: Volatile organic compounds (VOCs) in photochemically aged air from the eastern and western Mediterranean. *Atmos. Chem. Phys.*, **17**, 9547–9566, https://doi.org/10.5194/acp-17-9547-2017.

Dhaka, S. K., and Coauthors, 2020: $PM_{2.5}$ diminution and haze events over Delhi during the COVID-19 lockdown period: An interplay between the baseline pollution and meteorology. *Sci. Rep.*, **10**, 13442, https://doi.org/10.1038/s41598-020-70179-8.

Dörich, R., P. Eger, J. Lelieveld, and J. N. Crowley, 2021: Iodide CIMS and *m/z* 62: The detection of HNO_3 as NO_3^- in the presence of PAN, peroxyacetic acid and ozone. *Atmos. Meas. Tech.*, **14**, 5319–5332, https://doi.org/10.5194/amt-14-5319-2021.

Drewnick, F., and Coauthors, 2005: A new Time-of-Flight Aerosol Mass Spectrometer (TOF-AMS): Instrument description and first field deployment. *Aerosol Sci. Technol.*, **39**, 637–658, https://doi.org/10.1080/02786820500182040.

Edtbauer, E., C. Stönner, E. Y. Pfannerstill, M. Berasategui, D. Walter, J. N. Crowley, J. Lelieveld, and J. Williams, 2020: A new marine biogenic emission: Methane sulfonamide (MSAM), dimethyl sulfide (DMS), and dimethyl sulfone ($DMSO_2$) measured in air over the Arabian Sea. *Atmos. Chem. Phys.*, **20**, 6081–6094, https://doi.org/10.5194/acp-20-6081-2020.

Emde, C., and Coauthors, 2016: The libRadtran software package for radiative transfer calculations (version 2.0.1). *Geosci. Model Dev.*, **9**, 1647–1672, https://doi.org/10.5194/gmd-9-1647-2016.

Erbertseder, T., and D. Loyola, 2020: Despite weather influence—Corona effect now indisputable. DLR Earth Observation Center, accessed 2 February 2021, www.dlr.de/eoc/en/desktopdefault.aspx/tabid-14195/24618_read-64626.

Feldpausch, P., M. Fiebig, L. Fritzsche, and A. S Petzold, 2006: Measurement of ultrafine aerosol size distributions by a combination of diffusion screen separators and condensation particle counters. *J. Aerosol Sci.*, **37**, 577–597, https://doi.org/10.1016/j.jaerosci.2005.04.009.

Feng, R., and Coauthors, 2021: Quantifying air pollutant variations during COVID-19 lockdown in a capital city in northwest China. *Atmosphere*, **12**, 788, https://doi.org/10.3390/atmos12060788.

Fenn, R. W., and Coauthors, 1985: Optical and infrared properties of the atmosphere. Handbook of geophysics and space environment, Air Force Geophysics Laboratory Doc., www.cnofs.org/Handbook_of_Geophysics_1985/pdf_menu.htm.

Fiebig, M., C. Stein, F. Schröder, P. Feldpausch, and A. Petzold, 2005: Inversion of data containing information on the aerosol particle size distribution using multiple instruments. *J. Aerosol Sci.*, **36**, 1353–1372, https://doi.org/10.1016/j.jaerosci.2005.01.004.

Forster, P. M., and Coauthors, 2020: Current and future global climate impacts resulting from COVID-19. *Nat. Climate. Change*, **10**, 913–919, https://doi.org/10.1038/s41558-020-0883-0.

Georgoulias, A. K., R. J. van der A, P. Stammes, K. F. Boersma, and H. J. Eskes, 2019: Trends and trend reversal detection in 2 decades of tropospheric NO_2 satellite observations. *Atmos. Chem. Phys.*, **19**, 6269–6294, https://doi.org/10.5194/acp-19-6269-2019.

Gettelman, A., C.-C. Chen, and C. G. Bardeen, 2021: The climate impact of COVID-19-induced contrail changes. *Atmos. Chem. Phys.*, **21**, 9405–9416, https://doi.org/10.5194/acp-21-9405-2021.

Goldberg, D. L., S. C. Anenberg, D. Griffin, C. A. McLinden, Z. Lu, and D. G. Streets, 2020: Disentangling the impact of the COVID-19 lockdowns on urban NO^2 from natural variability. *Geophys. Res. Lett.*, **47**, e2020GL089269, https://doi.org/10.1002/essoar.10503396.1.

Grewe, V., E. Tsati, M. Mertens, C. Frömming, and P. Jöckel, 2017: Contribution of emissions to concentrations: the TAGGING 1.0 submodel based on the Modular Earth Submodel System (MESSy 2.52). *Geosci. Model Dev.*, **10**, 2615–2633, https://doi.org/10.5194/gmd-10-2615-2017.

Guevara, M., O. Jorba, H. Petetin, A. Nicodemou, and I. Jiménez, 2020: D8: Scientific content explaining the main outcomes of the project and data analysis. ECMWF Copernicus Rep. CAMS/COP_066, 24 pp., https://atmosphere.copernicus.eu/sites/default/files/2020-12/CAMS_COP_066_2020SC1_D8_202012_v1.pdf.

——, and Coauthors, 2021: Time-resolved emission reductions for atmospheric chemistry modelling in Europe during the COVID-19 lockdowns. *Atmos. Chem. Phys.*, **21**, 773–797, https://doi.org/10.5194/acp-21-773-2021.

Hallar, A. G., and Coauthors, 2021: Coupled air quality and boundary-layer meteorology in western U.S. basins during winter: Design and rationale for a

Brought to you by TU DELFT | Unauthenticated | Downloaded 11/07/22 01:10 PM UTC

comprehensive study. *Bull. Amer. Meteor. Soc.*, **102**, E2012–E2033, https://doi.org/10.1175/BAMS-D-20-0017.1.

Heller, R., and Coauthors, 2017: Mountain waves modulate the water vapor distribution in the UTLS. *Atmos. Chem. Phys.*, **17**, 14853–14869, https://doi.org/10.5194/acp-17-14853-2017.

Heymsfield, A. J., D. Baumgardner, P. DeMott, P. Forster, K. Gierens, and B. Kärcher, 2010: Contrail microphysics. *Bull. Amer. Meteor. Soc.*, **91**, 465–472, https://doi.org/10.1175/2009BAMS2839.1.

Holanda, B. A., and Coauthors, 2020: Influx of African biomass burning aerosol during the Amazonian dry season through layered transatlantic transport of black carbon-rich smoke. *Atmos. Chem. Phys.*, **20**, 4757–4785, https://doi.org/10.5194/acp-20-4757-2020.

Höpfner, M., and Coauthors, 2015: Sulfur dioxide (SO_2) from MIPAS in the upper troposphere and lower stratosphere 2002–2012. *Atmos. Chem. Phys.*, **15**, 7017–7037, https://doi.org/10.5194/acp-15-7017-2015.

Hosaynali Beygi, Z., and Coauthors, 2011: Oxidation photochemistry in the southern Atlantic boundary layer: Unexpected deviations from photochemical steady state. *Atmos. Chem. Phys.*, **11**, 8497–8513, https://doi.org/10.5194/acp-11-8497-2011.

Hottmann, B., and Coauthors, 2020: Impact of the South Asian monsoon outflow on atmospheric hydroperoxides in the upper troposphere. *Atmos. Chem. Phys.*, **20**, 12655–12673, https://doi.org/10.5194/acp-20-12655-2020.

Jöckel, P., and Coauthors, 2010: Development cycle 2 of the Modular Earth Submodel System (MESSy2). *Geosci. Model Dev.*, **3**, 717–752, https://doi.org/10.5194/gmd-3-717-2010.

Jurkat, T., and Coauthors, 2010: Airborne stratospheric ITCIMS measurements of SO_2, HCl, and HNO_3 in the aged plume of Volcano Kasatochi. *J. Geophys. Res.*, **115**, D00L17, https://doi.org/10.1029/2010JD013890.

——, S. Kaufmann, C. Voigt, D. Schäuble, P. Jeßberger, and H. Ziereis, 2016: The airborne mass spectrometer AIMS—Part 2: Measurements of trace gases with stratospheric or tropospheric origin in the UTLS. *Atmos. Meas. Tech.*, **9**, 1907–1923, https://doi.org/10.5194/amt-9-1907-2016.

——, and Coauthors, 2017: Depletion of ozone and reservoir species of chlorine and nitrogen oxide in the lower Antarctic polar vortex measured from aircraft. *Geophys. Res. Lett.*, **44**, GRL55959, https://doi.org/10.1002/2017GL073270.

Karle, N. N., R. M. Fitzgerald, R. K. Sakai, D. W. Sullivan, and W. R. Stockwell, 2021: Multi-scale atmospheric emissions, circulation and meteorological drivers of ozone episodes in El Paso-Juárez airshed. *Atmosphere*, **12**, 1575, https://doi.org/10.3390/atmos12121575.

Kaufmann, S., C. Voigt, P. Jeßberger, T. Jurkat, H. Schlager, A. Schwarzenboeck, M. Klingebiel, and T. Thornberry, 2014: In situ measurements of ice saturation in young contrails. *Geophys. Res. Lett.*, **41**, 702–709, https://doi.org/10.1002/2013GL058276.

——, and Coauthors, 2018: Intercomparison of mid-latitude tropospheric and lower stratospheric water vapor measurements and comparison to ECMWF humidity data. *Atmos. Chem. Phys.*, **18**, 16729–16745, https://doi.org/10.5194/acp-18-16729-2018.

Kerkweg, A., and P. Jöckel, 2012a: The 1-way on-line coupled atmospheric chemistry model system MECO(n)—Part 1: Description of the limited-area atmospheric chemistry model COSMO/MESSy. *Geosci. Model Dev.*, **5**, 87–110, https://doi.org/10.5194/gmd-5-87-2012.

——, and ——, 2012b: The 1-way on-line coupled atmospheric chemistry model system MECO(n)—Part 2: On-line coupling with the Multi-Model-Driver (MMD). *Geosci. Model Dev.*, **5**, 111–128, https://doi.org/10.5194/gmd-5-111-2012.

Klausner, T., and Coauthors, 2020: Urban greenhouse gas emissions from the Berlin area: A case study using airborne CO_2 and CH_4 in situ observations in summer 2018. *Elementa*, **8**, 15, https://doi.org/10.1525/elementa.411.

Kleine, J., and Coauthors, 2018: In situ observations of ice particle losses in a young persistent contrail. *Geophys. Res. Lett.*, **45**, 13553–13561, https://doi.org/10.1029/2018GL079390.

Kroll, J., C. Heald, C. Cappa, D. Farmer, J. Fry, J. G. Murphy, and A. Steiner, 2020: The complex chemical effects of COVID-19 shutdowns on air quality. *Nat. Chem.*, **12**, 777–779, https://doi.org/10.1038/s41557-020-0535-z.

Krüger, O., and Coauthors, 2022: Black carbon aerosol reductions during COVID-19 confinement quantified by aircraft measurements over Europe. *Atmos. Chem. Phys.*, **22**, 8683–8699, https://doi.org/10.5194/acp-22-8683-2022.

Le, T., Y. Wang, L. Liu, J. Yang, Y. L. Yung, G. Li, and J. H. Seinfeld, 2020: Unexpected air pollution with marked emission reductions during the COVID-19 outbreak in China. *Science*, **369**, 702–706, https://doi.org/10.1126/science.abb7431.

Lee, D. S., and Coauthors, 2010: Transport impacts on atmosphere and climate: Aviation. *Atmos. Environ.*, **44**, 4678–4734, https://doi.org/10.1016/j.atmosenv.2009.06.005.

——, and Coauthors, 2021: The contribution of global aviation to anthropogenic climate forcing for 2000 to 2018. *Atmos. Environ.*, **244**, 117834, https://doi.org/10.1016/j.atmosenv.2020.117834.

Le Quéré, C., and Coauthors, 2020: Temporary reduction in daily global CO_2 emissions during the COVID-19 forced confinement. *Nat. Climate Change*, **10**, 647–653, https://doi.org/10.1038/s41558-020-0797-x.

Li, Q., and S. Groß, 2021: Changes in cirrus cloud properties and occurrence over Europe during the COVID-19-caused air traffic reduction. *Atmos. Chem. Phys.*, **21**, 14573–14590, https://doi.org/10.5194/acp-21-14573-2021.

Liu, F., and Coauthors, 2020: Abrupt decline in tropospheric nitrogen dioxide over China after the outbreak of COVID-19. *Sci. Adv.*, **6**, eabc2992, https://doi.org/10.1126/sciadv.abc2992.

Lu, X., and Coauthors, 2021: The underappreciated role of agricultural soil nitrogen oxide emissions in ozone pollution regulation in North China. *Nat. Commun.*, **12**, 5021, https://doi.org/10.1038/s41467-021-25147-9.

Marno, D., and Coauthors, 2020: Calibration of an airborne HO_x instrument using the All Pressure Altitude-based Calibrator for HO_x Experimentation (APACHE). *Atmos. Meas. Tech.*, **13**, 2711–2731, https://doi.org/10.5194/amt-13-2711-2020.

Marsing, A., and Coauthors, 2019: Chlorine partitioning in the lowermost Arctic vortex during the cold winter 2015/2016. *Atmos. Chem. Phys.*, **19**, 10757–10772, https://doi.org/10.5194/acp-19-10757-2019.

Mayer, B., and A. Kylling, 2005: Technical note: The libRadtran software package for radiative transfer calculations—Description and examples of use. *Atmos. Chem. Phys.*, **5**, 1855–1877, https://doi.org/10.5194/acp-5-1855-2005.

Mertens, M., A. Kerkweg, P. Jöckel, H. Tost, and C. Hofmann, 2016: The 1-way on-line coupled model system MECO(n)—Part 4: Chemical evaluation (based on MESSy v2.52). *Geosci. Model Dev.*, **9**, 3545–3567, https://doi.org/10.5194/gmd-9-3545-2016.

——, ——, V. Grewe, P. Jöckel, and R. Sausen, 2020: Are contributions of emissions to ozone a matter of scale?—A study using MECO(n) (MESSy v2.50). *Geosci. Model Dev.*, **13**, 363–383, https://doi.org/10.5194/gmd-13-363-2020.

Minnis, P., and Coauthors, 2013: Linear contrail and contrail cirrus properties determined from satellite data. *Geophys. Res. Lett.*, **40**, 3220–3226, https://doi.org/10.1002/grl.50569.

Müller, I., T. Erbertseder, and H. Taubenböck, 2022: Tropospheric NO_2: Explorative analyses of spatial variability and impact factors. *Remote Sens. Environ.*, **270**, 112839, https://doi.org/10.1016/j.rse.2021.112839.

Munro, R., and Coauthors, 2016: The GOME-2 instrument on the MetOp series of satellites: Instrument design, calibration, and level 1 data processing—An overview. *Atmos. Meas. Tech.*, **9**, 1279–1301, https://doi.org/10.5194/amt-9-1279-2016.

Muser, L. O., and Coauthors, 2020: Particle aging and aerosol–radiation interaction affect volcanic plume dispersion: Evidence from the Raikoke 2019 eruption. *Atmos. Chem. Phys.*, **20**, 15015–15036, https://doi.org/10.5194/acp-20-15015-2020.

Pérez-Invernón, F. J., and Coauthors, 2022: Quantification of lightning-produced NO_x over the Pyrenees and the Ebro valley by using different TROPOMI-NO_2 and cloud research products. *Atmos. Meas. Tech.*, **15**, 3329–3351, https://doi.org/10.5194/amt-15-3329-2022.

Petit, J.-E., and Coauthors, 2021: Response of atmospheric composition to COVID-19 lockdown measures during spring in the Paris region (France). *Atmos. Chem. Phys.*, **21**, 17167–17183, https://doi.org/10.5194/acp-21-17167-2021.

Brought to you by TU DELFT | Unauthenticated | Downloaded 11/07/22 01:10 PM UTC

Petzoldt, K., 2010: On the climatology of nitrogen oxides, ozone, and carbon monoxide in the troposphere: An analysis of the MOZAIC data set (in German). Research Centrum Jülich Rep. 4327, 80 pp.

Phillips, G. J., and Coauthors, 2013: Peroxyacetyl nitrate (PAN) and peroxyacetic acid (PAA) measurements by iodide chemical ionisation mass spectrometry: First analysis of results in the boreal forest and implications for the measurement of PAN fluxes. *Atmos. Chem. Phys.*, **13**, 1129–1139, https://doi.org/10.5194/acp-13-1129-2013.

Putaud, J.-P., L. Pozzoli, E. Pisoni, S. Martins Dos Santos, F. Lagler, G. Lanzani, U. Dal Santo, and A. Colette, 2021: Impacts of the COVID-19 lockdown on air pollution at regional and urban background sites in northern Italy. *Atmos. Chem. Phys.*, **21**, 7597–7609, https://doi.org/10.5194/acp-21-7597-2021.

Quaas, J., E. Gryspeerdt, R. Vautard, and O. Boucher, 2021: Climate impact of aircraft-induced cirrus assessed from satellite observations before and during COVID-19. *Environ. Res. Lett.*, **16**, 064051, https://doi.org/10.1088/1748-9326/abf686.

Reifenberg, S. F., and Coauthors, 2022: Impact of reduced emissions on direct and indirect aerosol radiative forcing during COVID-19 lockdown in Europe. *Atmos. Chem. Phys*., https://doi.org/10.5194/acp-2021-1005, in press.

Schiller, C. L., H. Bozem, C. Gurk, U. Parchatka, R. Königstedt, G.W. Harris, J. Lelieveld, and H. Fischer, 2008: Applications of quantum cascade lasers for sensitive trace gas measurements of CO, CH_4, N_2O and HCHO. *Appl. Phys.*, **92B**, 419–430, https://doi.org/10.1007/s00340-008-3125-0.

Schlager, H., and Coauthors, 1997: In situ observations of air traffic emission signatures in the North Atlantic flight corridor. *J. Geophys. Res. Atmos.*, **102**, 10 739–10 750, https://doi.org/10.1029/96JD03748.

Schmale, J., and Coauthors, 2010: Aerosol layers from the 2008 eruptions of Mount Okmok and Mount Kasatochi: In situ upper troposphere and lower stratosphere measurements of sulfate and organics over Europe. *J. Geophys. Res.*, **115**, D00l07, https://doi.org/10.1029/2009JD013628.

Schulte, P., and H. Schlager, 1996: In-flight measurements of cruise altitude nitric oxide emission indices of commercial jet aircraft. *Geophys. Res. Lett.*, **23**, 165–168, https://doi.org/10.1029/95GL03691.

Schulz, C., and Coauthors, 2018: Aircraft-based observations of isoprene-epoxydiol-derived secondary organic aerosol (IEPOX-SOA) in the tropical upper troposphere over the Amazon region. *Atmos. Chem. Phys.*, **18**, 14 979–15 001, https://doi.org/10.5194/acp-18-14979-2018.

Schumann, U., 1996: On conditions for contrail formation from aircraft exhausts. *Meteor. Z.*, **5**, 4–23, https://doi.org/10.1127/metz/5/1996/4.

——, 2012: A contrail cirrus prediction model. *Geosci. Model Dev.*, **5**, 543–580, https://doi.org/10.5194/gmd-5-543-2012.

——, and K. Graf, 2013: Aviation-induced cirrus and radiation changes at diurnal timescales. *J. Geophys. Res.*, **118**, 2404–2421, https://doi.org/10.1002/jgrd.50184.

——, and A. J. Heymsfield, 2017: On the lifecycle of individual contrails and contrail cirrus. *Ice Formation and Evolution in Clouds and Precipitation: Measurement and Modeling Challenges*, *Meteor. Monogr.*, No. 58, Amer. Meteor. Soc., https://doi.org/10.1175/AMSMONOGRAPHS-D-16-0005.1.

——, and Coauthors, 2017: Properties of individual contrails: A compilation of observations and some comparisons. *Atmos. Chem. Phys.*, **17**, 403–438, https://doi.org/10.5194/acp-17-403-2017.

——, L. Bugliaro, A. Dörnbrack, R. Baumann, and C. Voigt, 2021a: Aviation contrail cirrus and radiative forcing over Europe during 6 months of COVID-19. *Geophys. Res. Lett.*, **48**, e2021GL092771, https://doi.org/10.1029/2021GL092771.

——, and Coauthors, 2021b: Air traffic and contrail changes over Europe during COVID-19: A model study. *Atmos. Chem. Phys.*, **21**, 7429–7450, https://doi.org/10.5194/acp-21-7429-2021.

Slusher, D. L., L. G. Huey, D. J. Tanner, F. M. Flocke, and J. M. Roberts, 2004: A thermal dissociation-chemical ionization mass spectrometry (TD-CIMS) technique for the simultaneous measurement of peroxyacyl nitrates and dinitrogen pentoxide. *J. Geophys. Res.*, **109**, D19315, https://doi.org/10.1029/2004JD004670.

Solimini, A., F. Filipponi, D. A. Fegatelli, B. Caputo, C. M. De Marco, A. Spagnoli, and A. R. Vestri, 2021: A global association between COVID-19 cases and airborne particulate matter at regional level. *Sci. Rep.*, **11**, 6256, https://doi.org/10.1038/s41598-021-85751-z.

Speidel, M., R. Nau, F. Arnold, H. Schlager, and A. Stohl, 2007: Sulfur dioxide measurements in the lower, middle and upper troposphere: Deployment of an aircraft-based chemical ionization mass spectrometer with permanent in-flight calibration. *Atmos. Environ.*, **41**, 2427–2437, https://doi.org/10.1016/j.atmosenv.2006.07.047.

Stephens, G., D. Winker, J. Pelon, C. Trepte, D. Vane, C. Yuhas, T. L'Ecuyer, and M. Lebsock, 2018: *CloudSat* and *CALIPSO* within the A-Train: Ten years of actively observing the Earth system. *Bull. Amer. Meteor. Soc.*, **99**, 569–581, https://doi.org/10.1175/BAMS-D-16-0324.1.

Strandgren, J., L. Bugliaro, F. Sehnke, and L. Schröder, 2017: Cirrus cloud retrieval with MSG/SEVIRI using artificial neural networks. *Atmos. Meas. Tech.*, **10**, 3547–3573, https://doi.org/10.5194/amt-10-3547-2017.

Tadic, I., and Coauthors, 2021: Central role of nitric oxide in ozone production in the upper tropical troposphere over the Atlantic Ocean and West Africa. *Atmos. Chem. Phys.*, **21**, 8195–8211, https://doi.org/10.5194/acp-21-8195-2021.

Taylor, J. W., and Coauthors, 2019: Aerosol influences on low-level clouds in the West African monsoon. *Atmos. Chem. Phys.*, **19**, 8503–8522, https://doi.org/10.5194/acp-19-8503-2019.

Teoh, R., U. Schumann, A. Majumdar, and M. E. J. Stettler, 2020: Mitigating the climate forcing of aircraft contrails by small-scale diversions and technology adoption. *Environ. Sci. Technol.*, **54**, 2941–2950, https://doi.org/10.1021/acs.est.9b05608.

Tesche, M., P. Achtert, P. Glantz, and K. J. Noone, 2016: Aviation effects on already-existing cirrus clouds. *Nat. Commun.*, **7**, 12016, https://doi.org/10.1038/ncomms12016.

Urbanek, B., S. Groß, M. Wirth, C. Rolf, M. Krämer, and C. Voigt, 2018: High depolarization ratios of naturally occurring cirrus clouds near air traffic regions over Europe. *Geophys. Res. Lett.*, **45**, 13 166–13 172, https://doi.org/10.1029/2018GL079345.

van Geffen, J. H. G. M., H. J. Eskes, K. F. Boersma, J. D. Maasakkers, and J. P. Veefkind, 2019: TROPOMI ATBD of the total and tropospheric NO_2 data products. KNMI Rep. S5P-KNMI-L2-0005-RP, 86 pp., https://sentinel.esa.int/documents/247904/2476257/Sentinel-5P-TROPOMI-ATBD-NO2-data-products.

van Heerwaarden, C., and Coauthors, 2021: Record high solar irradiance in western Europe during first COVID-19 lockdown largely due to unusual weather. *Nat. Commun. Earth Environ.*, **2**, 37, https://doi.org/10.1038/s43247-021-00110-0.

Vázquez-Navarro, M., H. Mannstein, and S. Kox, 2015: Contrail life cycle and properties from 1 year of MSG/SEVIRI rapid-scan images. *Atmos. Chem. Phys.*, **15**, 8739–8749, https://doi.org/10.5194/acp-15-8739-2015.

Veefkind, J. P., and Coauthors, 2012: TROPOMI on the ESA Sentinel-5 Precursor: A GMES mission for global observations of the atmospheric composition for climate, air quality and ozone layer applications. *Remote Sens. Environ.*, **120**, 70–83, https://doi.org/10.1016/j.rse.2011.09.027.

Venter, Z. S., K. Aunan, S. Chowdhury, and J. Lelieveld, 2020: COVID-19 lockdowns cause global air pollution declines. *Proc. Natl. Acad. Sci. USA*, **117**, 18 984–18 990, https://doi.org/10.1073/pnas.2006853117.

Virkkula, A., 2010: Correction of the calibration of the 3-wavelength Particle Soot Absorption Photometer (3λ PSAP). *Aerosol Sci. Technol.*, **44**, 706–712, https://doi.org/10.1080/02786826.2010.482110.

——, N. C. Ahlquist, D. S. Covert, W. P. Arnott, P. J. Sheridan, P. K. Quinn, and D. J. Coffman, 2005: Modification, calibration and a field test of an instrument for measuring light absorption by particles. *Aerosol Sci. Technol.*, **39**, 68–83, https://doi.org/10.1080/027868290901963.

Voigt, C., and Coauthors, 2010: In-situ observations of young contrails—Overview and selected results from the CONCERT campaign. *Atmos. Chem. Phys.*, **10**, 9039–9056, https://doi.org/10.5194/acp-10-9039-2010.

——, and Coauthors, 2011: Extinction and optical depth of contrails. *Geophys. Res. Lett.*, **38**, L11806, https://doi.org/10.1029/2011GL047189.

——, and Coauthors, 2014: Evolution of CO_2, SO_2, HCl and HNO_3 in the volcanic plumes from Etna. *Geophys. Res. Lett.*, **41**, 2196–2203, https://doi.org/10.1002/2013GL058974.

Brought to you by TU DELFT | Unauthenticated | Downloaded 11/07/22 01:10 PM UTC

——, and Coauthors, 2017: ML-CIRRUS: The airborne experiment on natural cirrus and contrail cirrus with the High-Altitude Long-Range Research Aircraft HALO. *Bull. Amer. Meteor. Soc.*, **98**, 271–288, https://doi.org/10.1175/BAMS-D-15-00213.1.

——, and Coauthors, 2021: Cleaner burning aviation fuels can reduce contrail cloudiness. *Nat. Commun. Earth Environ.*, **2**, 114, https://doi.org/10.1038/s43247-021-00174-y.

Williamson, C. J., and Coauthors, 2021: Large hemispheric difference in nucleation mode aerosol concentrations in the lowermost stratosphere at mid- and high latitudes. *Atmos. Chem. Phys.*, **21**, 9065–9088, https://doi.org/10.5194/acp-21-9065-2021.

Winker, D. M., B. H. Hunt, and M. J. McGill, 2007: Initial performance assessment of CALIOP. *Geophys. Res. Lett.*, **34**, L19803, https://doi.org/10.1029/2007GL030135.

——, and Coauthors, 2010: The *CALIPSO* mission: A global 3D view of aerosols and clouds. *Bull. Amer. Meteor. Soc.*, **91**, 1211–1229, https://doi.org/10.1175/2010BAMS3009.1.

Zahn, A., J. Weppner, H. Widmann, K. Schlote-Holubek, B. Burger, T. Kühner, and H. Franke, 2012: A fast and precise chemiluminescence ozone detector for eddy flux and airborne application. *Atmos. Meas. Tech.*, **5**, 363–375, https://doi.org/10.5194/amt-5-363-2012.

Zhou, Y., D. Brunner, C. Hueglin, S. Henne, and J. Staehelin, 2012: Changes in OMI tropospheric NO_2 columns over Europe from 2004 to 2009 and the influence of meteorological variability. *Atmos. Environ.*, **46**, 482–495, https://doi.org/10.1016/j.atmosenv.2011.09.024.

Ziereis, H., H. Schlager, P. Schulte, P. van Velthoven, and F. Slemr, 2000: Distributions of NO, NO_x, and NO_y in the upper troposphere and lower stratosphere between 28° and 61°N during POLINAT 2. *J. Geophys. Res.*, **105**, 3653–3664, https://doi.org/10.1029/1999JD900870.

——, and Coauthors, 2022: Redistribution of total reactive nitrogen in the lowermost Arctic stratosphere during the cold winter 2015/2016. *Atmos. Chem. Phys.*, **22**, 3631–3654, https://doi.org/10.5194/acp-22-3631-2022.

Brought to you by TU DELFT | Unauthenticated | Downloaded 11/07/22 01:10 PM UTC